THE ASTRONOMICAL JOURNAL, 117:792–810, 1999 February

THE STRUCTURE AND DYNAMICS OF THE EARLY-TYPE RESONANCE RING GALAXY IC 4214. II. MODELS

H. SALO,[1] P. RAUTIAINEN,[1] R. BUTA,[2,3] GUY B. PURCELL,[2,3] MELINDA LEWIS COBB,[4]
D. A. CROCKER,[2,3] AND E. LAURIKAINEN[1]
Received 1998 June 1; accepted 1998 October 12

ABSTRACT

The first paper in this series presented optical (*UBVI*) and near-infrared (*H*) surface photometry and Hα Fabry-Perot interferometry of IC 4214, an excellent example of a multiringed galaxy with a weak bar. In the present paper, we analyze the nonaxisymmetric gravitational potential of IC 4214, as defined by the near-infrared data. The gas behavior is modeled with two-dimensional sticky particle simulations that employ a rigidly rotating nonaxisymmetric potential. Our goals are to interpret the morphology and velocity field of IC 4214 and to obtain a model from which the bar pattern speed, halo contribution, and relative bulge and disk masses can be deduced. We also study the orbital families in the derived IC 4214 model.

A fairly good match, in both morphology and kinematics, is obtained for $\Omega_{\rm bar} \approx 40 \pm 5$ km s^{-1} kpc^{-1}, placing the bar corotation slightly beyond the end of the bar ($r_{\rm bar}/r_{\rm cr} \approx 0.72 \pm 0.05$). The deduced bar amplitude implies that the visible mass of the disk dominates over the unseen halo ($M_{\rm disk}/M_{\rm halo} > 3$–4). Moreover, our model accounts quantitatively for the large difference in the orientation of IC 4214 as derived in our first paper with photometric and kinematic methods.

Key words: galaxies: individual (IC 4214) — galaxies: kinematics and dynamics — galaxies: photometry — galaxies: structure

1. INTRODUCTION

Many different aspects of the dynamics of barred galaxies have been studied, including the formation, evolution, and possible destruction of bars. The ring structures and their relation to resonances have also received much attention. (For a detailed review of various studies, see Sellwood & Wilkinson 1993 and Buta & Combes 1996.) The most challenging way to check the results of dynamical studies is to model observed individual galaxies, the main goal being the determination of the mass distribution of the system and the pattern speed of the bar.

There have been several attempts to relate the bar pattern speed to its extent. The analysis of orbits in barred potentials indicates that a bar cannot extend beyond its own corotation resonance, or to the region where the bar rotation speed would exceed the local angular speed, owing to the lack of supporting orbits (Contopoulos 1980; Contopoulos & Grosbøl 1989). In other words, this gives the maximal possible pattern speed. Indeed, some *N*-body models suggest that the end of the bar is located very near corotation or $r_{\rm bar} \simeq r_{\rm cr}$ (Sellwood 1981), whereas gas-dynamical models of leading offset dust lanes seem to favor a slightly lower value, around $r_{\rm bar} \simeq 0.8 r_{\rm cr}$ (Athanassoula 1992b). On the other hand, Combes & Elmegreen (1993) presented a simulation where a strong bar ends near its inner Lindblad resonance ($r_{\rm bar} \ll r_{\rm cr}$) and proposed this to be typical for late-type spirals. However, the initial parameters they used are not necessarily realistic (Sellwood 1996).

Rings and pseudorings are considered to be good indicators of resonances and, if the rotation curve is known, also of the pattern speed. Studies in which ring formation is simulated (Schwarz 1981; Combes & Gerin 1985; Byrd et al. 1994; Piner, Stone, & Teuben 1995) suggest that outer rings are related to outer Lindblad resonances (OLR) and nuclear rings to inner Lindblad resonances (ILR). The major axis of the inner ring can be near the corotation resonance, although these rings are considered to be related to the inner 4/1 ultraharmonic resonance (UHR). As shown by Buta et al. (1995) in modeling NGC 7217, even a slight and hard-to-detect deviation from axisymmetry can account for the observed ring morphology. In practice, the identification of resonances is often complicated by the fact that their exact locations are significantly affected by the strength of the nonaxisymmetric perturbation.

During recent years, several individual barred galaxies have been modeled, some even more than once. The results from these studies are fairly consistent with respect to the pattern speed, and the bar usually seems to end near the deduced corotation distance. In most cases the observed morphology and kinematics could not be fully explained with only the bar component present. This deficiency has been explained either by supposing an unseen oval component outside the bar (Hunter et al. 1988; England 1989; Ball 1992) or, more elegantly, by a spiral potential deduced from the observations (Lindblad, Lindblad, & Athanassoula 1996; Lindblad & Kristen 1996).

IC 4214 is an early-type weakly barred galaxy possessing all basic ring types: outer, inner, and nuclear. The outer pseudoring is of type R'_1 (Buta 1995), which means that it is defined by two spiral arms that wind about 180° with respect to the ends of the bar. The inner ring is also defined by spiral structure. In barred galaxies, R'_1 pseudorings are aligned perpendicular to the bar on average, whereas inner

[1] Department of Physical Sciences, Division of Astronomy, University of Oulu, FIN-90570 Oulu, Finland.
[2] Department of Physics and Astronomy, University of Alabama, Tuscaloosa, AL 35487-0324.
[3] Visiting Astronomer, Cerro Tololo Inter-American Observatory, National Optical Astronomy Observatories, which is operated by the Association of Universities for Research in Astronomy (AURA), Inc., under cooperative agreement with the National Science Foundation.
[4] Department of Physics and Astronomy, Muskingum College, New Concord, OH 43762.

rings and pseudorings are aligned parallel to the bar. The nuclear ring of IC 4214 is not oriented either perpendicular or parallel to the bar but is leading the bar by about 50°, which is fairly typical. The orientation of a barred galaxy has a strong influence on how well the noncircular velocities are manifested in the observed velocity field (Athanassoula 1984; Pence & Blackman 1984). IC 4214 is suitably oriented (bar major axis neither parallel nor perpendicular to the galaxy major axis) so that the Fabry-Perot Hα velocity field shows distinct signs of noncircular velocities. This is essential for comparing models with observations. Another factor making IC 4214 an ideal candidate for numerical modeling is the fact that its bar is rather weak: for example, this makes the identification of kinematic resonance signatures more reliable.

Numerous N-body simulations have indicated that an initially axisymmetric disk evolves rapidly into a barred configuration through a global instability, provided that the disk velocity dispersion is not too high and that the disk contributes at least about one-half to the total force field (see, e.g., Ostriker & Peebles 1973). The modeling of gas features in individual barred galaxies with a full N-body simulation is thus rather problematic, as the details of the final outcome are difficult to control via initial conditions. Another approach is to determine the gravitational potential from observations and explore the response of gas on a rigidly rotating nonaxisymmetric component. This has been the method used by Lindblad et al. (1996). However, even with this simplified approach several free parameters remain, including the disk and bulge mass-to-luminosity ratio, the disk and bar three-dimensional density distributions, and the pattern speed of the bar. Also, it might turn out to be necessary to include an extended halo component, if required by the rotation curve. All these factors can be estimated by detailed comparison of model predicted kinematic and morphological behavior with the observations. The main advantage of a rigid bar model is that each factor can be studied separately and fine-tuned as required by observations. Besides, because the amplitude of the assigned perturbation can be freely varied, the simulation results can be linked to analytical linear calculations.

In the present paper we study the gas response in a rigidly rotating potential derived from observations (Buta et al. 1998, hereafter Paper I). Sections 2 and 3 describe the simulation method and simulation tests with rigid and self-consistent bar potentials. The derivation of the IC 4214 potential from observations, as well as the uncertainties involved, are discussed in § 4. Section 5 describes our simulation survey, concentrating on estimating the bar strength and pattern speed. Simulation results are also interpreted in terms of families of closed periodic orbits. Section 6 applies various methods for the determination of the galaxy's orientation to the simulated data, with the aim of explaining the discrepancies between photometric and kinematic determinations of IC 4214's orientation parameters (Paper I). Our results and conclusions are summarized in § 7.

2. THE SIMULATION METHOD

The simulations of the present study employ the two-dimensional polar-grid code by Salo (1991; see Salo & Laurikainen 1993 for a description of their three-dimensional version). The gravitational potential of the disk is evaluated on a logarithmic polar grid, with $N_r = 144$ radial and $N_\theta = 108$ azimuthal divisions. Within the grid area the forces are obtained by interpolation from the potential: for IC 4214 with exponential scale length $r_e \approx 20''$, the grid covers $0''.25 < r < 1000''$. Very few particles fall inside the grid central hole: if this happens, forces are calculated with a direct summation from the tabulated density. The bulge force (and that due to the extended halo) is calculated either from an analytical formula or, if given in tabular form, with a much finer radial interpolation. In the current simulations with rigid bar potential, the axisymmetric component of the disk is added to the bulge (and halo) force, and the nonaxisymmetric, rigidly rotating potential needs to be evaluated only in the beginning of the run. However, the self-consistent method is utilized in the tests of § 3. Compared with the Byrd et al. (1994) rigid bar simulations using the same code, the difference is that the bar potential is now calculated from the observed density distribution instead of an analytical model.

The gas behavior is simulated by following 20,000 inelastically colliding test particles ("sticky particles"). Instead of using a grid-based collision scheme (Schwarz 1981), accurate collisions are searched during each time step as described in Salo (1991): this gives a better resolution of gas motions. In each collision, the perpendicular component of the relative velocity of the colliding pair is reversed and multiplied by the coefficient of restitution, α. As long as α is close to zero, the results are fairly insensitive to its exact value: in the present study we have set $\alpha = 0$, so that the cloud impacts are completely inelastic. Because of the extremely high cloud density obtained in some regions, e.g., nuclear rings, the impact search is restricted so that only one collision per particle is allowed during one time step. The purpose of this is to ensure that the simulation will not slow down intolerably as a result of extreme collision frequency in high-density regions. Self-gravitational effects of the gas component are not included.

Besides gas, also 200,000 test particle "stars" are included in some simulations. They are noncolliding and differ from gas particles also in having larger initial velocity dispersion and different radial distribution (exponential instead of uniform; initial radial velocity dispersion 10%–30% of the circular velocity as compared with 1% for the gas). They are used for some (very rough!) comparisons of expected and observed behavior of the stellar component.

The integrations are performed with a time-centered leapfrog integrator, with about 300 steps per bar rotation period (about 100 steps per revolution at the distance of the nuclear ring). The duration of each simulation is of the order of 10–30 bar rotation periods (corresponding to about 1.5–4 Gyr).

The gravitational potential of IC 4214 is estimated with the help of the near-infrared H-band data obtained in Paper I. We assume that the observed surface brightness distribution of IC 4214 represents also the surface density distribution of the disk component. Thus, after the bulge subtraction, the galaxy image is deprojected, assuming zero thickness, with the orientation parameters derived in Paper I. The various Fourier components of the disk surface density distribution are then calculated. The axisymmetric part of the gravitational potential σ_0 is calculated from the $m = 0$ Fourier component of surface density distribution, and the rotating part arising from the bar and spiral arms is represented by the even $m = 2$, 4, 6, 8, and 10 components. The odd components are not included in the simulation potential because, even if they were significant, they can

hardly be expected to possess the same pattern speed as the bar. The total surface density in simulations is thus expressed as

$$\sigma(r, \theta) = \sigma_0(r) + \sum \sigma_m(r) \cos \{m[\theta - \theta_m(r)]\} ,$$

where $\sigma_m(r)$ and $\theta_m(r)$ denote the amplitude and the phase of each Fourier component. A similar decomposition of the potential is used in the analysis of the gravitational field.

The three-dimensional structure of the bar and disk is taken into account by using softening in the calculation of gravitational forces, by replacing the Newtonian $1/\Delta$ potential with $1/\sqrt{\Delta^2 + \epsilon^2}$, where Δ denotes the distance from the gravitating mass element and ϵ the softening length (Sellwood 1987). The softened gravitational potential arising from the two-dimensional surface density distribution is practically indistinguishable from that with a vertical distribution and nonsoftened gravity, provided that ϵ is correctly related to the vertical distribution. In particular, if the vertical scale parameter z_0 is small (compared with radial scales of interest, e.g., r_e or bar length), then ϵ corresponds closely to z_0. Unless otherwise mentioned, $\epsilon = 2''.5$ is used in our simulations. The sole reason for representing three-dimensional structure with softened gravity is that this enables the accurate comparison of rigid bar simulations with two-dimensional live disk simulations (see § 3).

In each simulation, the nonaxisymmetric part of the potential is turned on gradually during one bar rotation period, to avoid transient features (Schwarz 1985). In addition to the disk potential, the spherically symmetric bulge potential corresponding to its projected surface density profile is calculated. In principle, the mass-to-luminosity ratio M/L_H of the bulge is allowed to differ from that of the disk.

In all models studied we assume that the bar and the spiral arms corotate. This means that our method fails if these are independent phenomena having different pattern speeds, as suggested by Sellwood & Sparke (1988). Our method would also be inadequate in the case of nonlinear coupling between the bar and outer spiral structure (Masset & Tagger 1997). Also, the method is only approximate in the sense that any possible time variability of the bar potential (most importantly, slowing down as a result of angular momentum transfer to an extended halo; see Little & Carlberg 1991; Debattista & Sellwood 1998) is omitted. Similarly, features resulting from three-dimensional gas motions are beyond the scope of the present simulations.

3. TESTING THE SIMULATION METHOD

Besides the trivial accuracy tests (e.g., results do not change if the integration time step is decreased or if the resolution of the potential grid is improved), several other checks were carried out with our rigid numerical bar simulation method. In particular, we wanted to make sure that its results agree with those of N-body simulations with "live" bars. We thus took the stellar density distribution from a barred end state of a two-dimensional N-body simulation and used this as a substitute for the H-band image in the potential evaluation. We then compared the evolution of the gas distributions in simulations with this frozen bar potential, with various pattern speeds and amplitudes. This is an accurate test because the parameters of the underlying bulge and disk are precisely known. Figure 1 compares an example of original gas distributions in the N-body run and that obtained in a simulation with a rigid bar potential. In addition to using the correct pattern speed ($\Omega_{\rm bar}$) and amplitude ($A_{\rm bar}$) of the N-body run, cases with too fast/slow or too weak/strong bars are also compared. The spiral structure and the size of the nuclear ring is indeed best matched with the correct pattern speed and amplitude, although in the example shown a slightly overestimated $\Omega_{\rm bar}$ would be difficult to rule out. In cases with a well-defined inner ring as in IC 4214, its morphology helps to limit both pattern speed and amplitude. In general, when the other parameters of the model are correct, both the amplitude and pattern speed can be determined with a modest (say, at least 25%) accuracy. We also inserted the gas particles from the rigid bar simulation back into the original N-body code: no transient effects were present, indicating that the kinematics are also well reproduced by the rigid bar method.

Some additional N-body test cases (corresponding to Fig. 1 but not shown) exhibited spiral structures also beyond the outer ring region. These features had lower pattern speeds than the bar and the inner spirals and, as expected, were not reproduced in rigid bar calculations using a single pattern speed appropriate for the inner regions. It has been suggested that the pattern speeds of spiral and bar components in general may be different (Sellwood & Sparke 1988), although this is probably not the case for galaxies with large-scale bars and/or outer rings (Rautiainen & Salo 1998). The parameters of the above-mentioned additional test cases were deliberately chosen in a manner that produces detached outer spirals, by using a very extended stellar distribution. However, this is not relevant in the case of IC 4214, which has no structure beyond the outer pseudoring. Our final models for IC 4214 (see § 5) are also consistent with a single pattern speed in common for the bar and the outer spirals.

The formation of ring structures in the gas component is a result of its viscous behavior. In the sticky particle simulations, viscosity is determined by the frequency of impacts between gas particles (in the two-dimensional case proportional to particle surface number density, particle radius, and velocity dispersion). It is difficult to relate the model parameters to the actual physical processes of the interstellar medium, and therefore our interest must be limited to robust features that are not sensitive to the exact amount of viscosity. Our standard cloud size ($0''.005 \approx 0.8$ pc) yields an initial impact frequency of the order of 0.3 impacts per cloud per one bar orbital revolution. Later, with the formation of rings, the impact frequency rises much higher, especially in the inner ring. Already a much smaller impact frequency would be sufficient for the formation of features such as nuclear rings, but then the other ring features would remain weak. On the other hand, extremely high impact frequency may lead to possibly unrealistic effects like strong clumps in the spiral arms. Between these extremes, the overall morphology does not depend strongly on the amount of viscosity, in agreement with Byrd et al. (1994).

However, even if the occurrence of various features seen in the simulations is not very sensitive to the gas cloud parameters, the timescale required for their formation is: increased viscosity speeds up the evolution. Because we employ an artificial initial distribution for gas (uniform initial distribution: this helps to bring out the outer rings), there is no guarantee that the relative amount of viscosity at various parts of the system is comparable to real systems. We must thus accept that the different features seen in simulation snapshots can in fact correspond to totally different

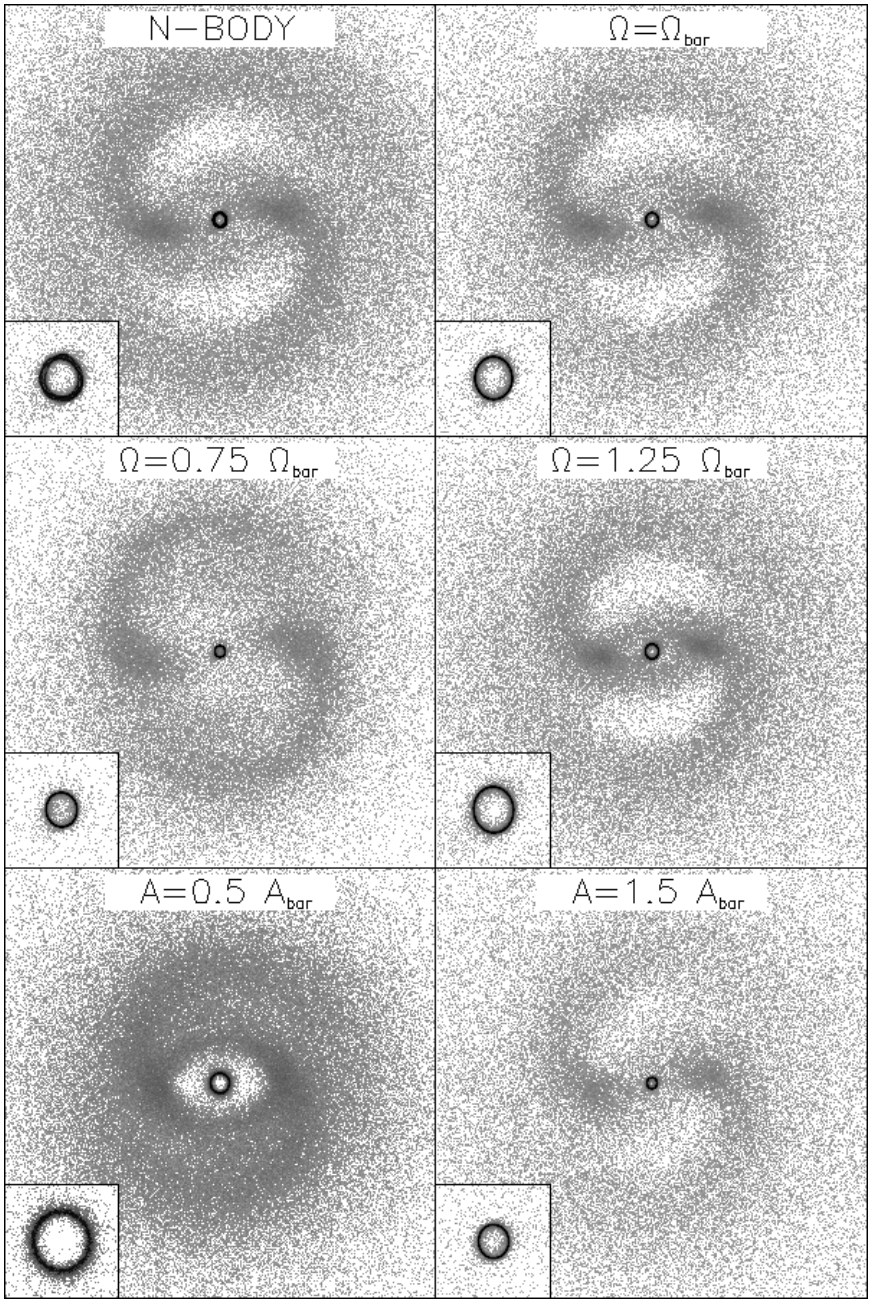

FIG. 1.—Test of the simulation method using a rigidly rotating bar potential. *Top left*: the gas distribution in a two-dimensional N-body simulation with a self-gravitating exponential star disk and an analytical Plummer bulge potential ($M_{\rm bulge}/M_{\rm disk} = 0.2$, $r_{\rm PL}/r_e = 0.2$, $\epsilon = 0.25 r_e$, initial $Q_{\rm T} = 1.5$). *Top right*: the gas distribution in a corresponding simulation with a rigidly rotating potential, with the pattern speed ($\Omega_{\rm bar}$) and bar amplitude ($A_{\rm bar}$) derived from the N-body simulation. The next two rows show results from rigid bar simulations where either $\Omega_{\rm bar}$ or $A_{\rm bar}$ has been varied. The density distribution and the gravitational potential of the N-body disk have been evaluated about five bar revolutions before the snapshots displayed in the figure. All other parameters (bulge parameters, gravity softening, gas cloud size) are identical. A uniform initial distribution of gas has been used in all models: initial velocities of rigid bar models have been interpolated from the N-body velocities in order to minimize transient effects due to the sudden introduction of the nonaxisymmetric potential. The inset displays the nuclear ring region with a threefold magnification.

physical timescales in different regions. In particular, the formation and eventual dispersal of spiral structures between the inner and nuclear rings has a very rapid timescale in our simulations. In actual systems the recycling between gas and stars could significantly affect the timescales (see, e.g., Friedli & Benz 1995) and help to maintain the inner spirals, as fresh gas would be continuously available. However, to keep our gas model as simple as possible, we have not included any recycling processes.

4. THE MODEL PARAMETERS OF IC 4214

In Paper I the inclination and position angle of IC 4214 were derived from observations, but there was considerable deviation between the results obtained by different methods, most likely due to nonaxisymmetric distortions induced by the bar. For example, photometric and kinematic methods suggest different inclinations, $i = 47°$ and $57°$, respectively, while the corresponding position angles

are $\phi = 175°$ and 169°. The requirement that the outer and inner rings are perpendicular yields $i = 52°$, if the position angle is fixed to the kinematic value. All the subsequent analysis (bulge/disk decomposition, bar amplitude) is to some degree affected by the uncertainty in orientation parameters, as discussed below. However, we show later (§ 6) that the differences between various determinations can be explained in terms of our simulations. Unless otherwise mentioned, the nominal values used in all the subsequent analysis and simulations are $(\phi, i) = (170°, 52°)$, close to the intermediate values favored in Paper I. The distance of IC 4214 is taken to be 31.6 Mpc, so that 1″ corresponds to 0.153 kpc.

4.1. *Axisymmetric Mass Model and Rotation Curve*

In Paper I the decomposition into a spherical bulge and a thin axisymmetric disk was performed with the method of Kent (1986). The obtained bulge (see Fig. 2*a*) is quite far from an $r^{1/4}$ distribution but is fairly well approximated by a Plummer sphere with a scale parameter $r_{\rm PL} = 2\farcs5$. However, the mass distribution resulting from this bulge/disk light decomposition cannot be made consistent with the observed rotation curve (Paper I), unless very large radial variations in the M/L_H ratio are allowed. This is illustrated by Figure 3*a*, which compares the observed inner rotation curve with that obtained from the above model with various constant M/L_H. Clearly, to explain the shallow slope of $V_{\rm rot}(r)$ within $r \approx 5''$, the M/L_H should be as low as 0.1 in this region, whereas to account for the maximal velocities, the overall $M/L_H \approx 0.75$. It might thus be possible that IC 4214 exhibits a nuclear starburst (for which $M/L_H \approx 0.1$; Oliva et al. 1995). This is also supported by the similarity of the observed H-band and Hα morphologies of the nuclear rings, which suggests a significant contribution of young stars in this region (Paper I).

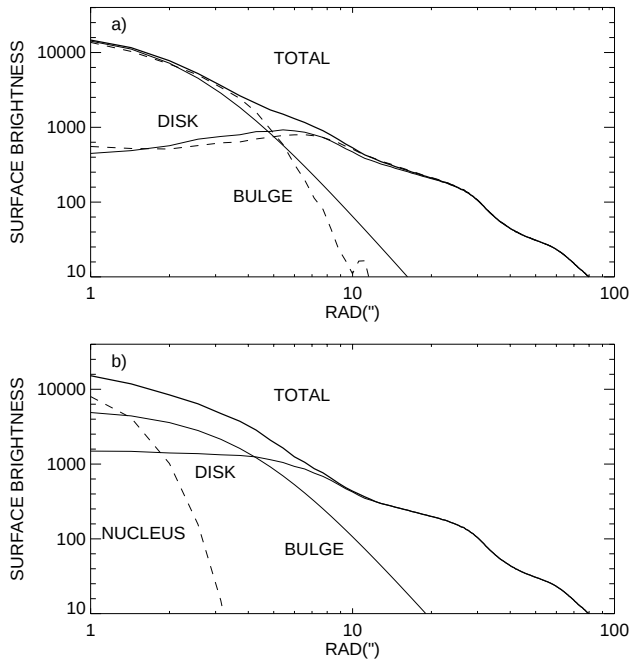

FIG. 2.—The bulge/disk decomposition for the IC 4214 H-band light distribution. In (*a*) the dashed lines indicate the decomposition into spherical bulge and thin disk with the Kent (1986) method, described in Paper I. Solid lines denote an approximate fit where a Plummer sphere distribution is used for the bulge, with scale radius $r_{\rm PL} = 2\farcs5$, and comprising about 23% of the total light. In (*b*) an alternative bulge/disk decomposition for IC 4214 is shown. The dashed line indicates a Gaussian profile corresponding to FWHM of 1.″96 for a nonresolved central source (comprising about 3% of total H-band light). The bulge is modeled with a Plummer sphere, with $r_{\rm PL} = 4''$ (17% of the total light). This is the mass model assumed in subsequent figures unless otherwise indicated.

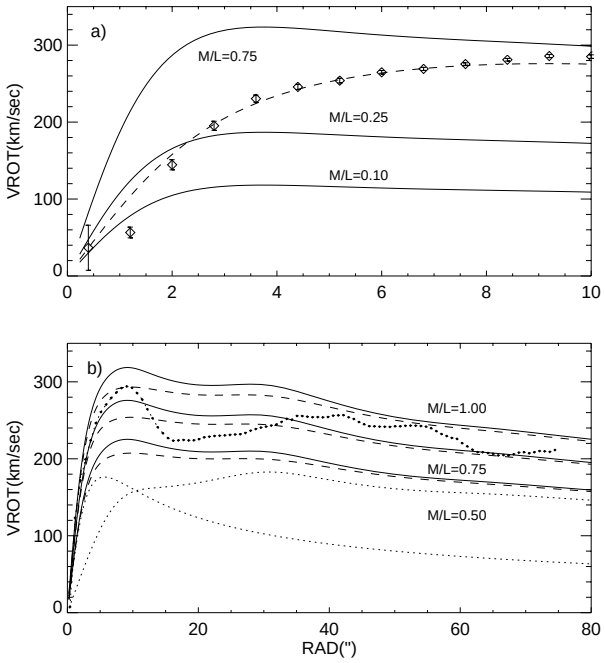

FIG. 3.—(*a*) Inner rotation curve following from the light distribution of Fig. 2*a*, with various constant values for the M/L_H ratio (*solid lines*; same M/L_H for the disk and the bulge). Symbols denote the azimuthally averaged rotation curve deduced from Hα observations (Paper I). For comparison, dashed lines represent the rotation curve derived from Fig. 2*b*, with $M/L_H = 0.75$ for the bulge and the disk, and with $M/L_H = 0$ for the nonresolved central source. (*b*) The overall rotation curve following from the light distribution of Fig. 2*b*, with various constant values for the M/L_H ratio (*solid lines*). Symbols denote the azimuthally averaged rotation curve deduced from Hα observations. Dotted lines denote separately the bulge and disk contributions in the case $M/L_H = 0.5$. Dashed lines refer to a thick bar model ($\epsilon = 5''$; for solid lines, $\epsilon = 2\farcs5$).

Figure 2*b* displays an example of an alternative disk/bulge decomposition, where we have first subtracted a nonresolved nuclear source (Gaussian in shape with an FWHM of 1.″72 on the H-band image, and comprising about 3% of the total H-band luminosity), and approximated the rest as a sum of a Plummer sphere and a thin axisymmetric disk. The resulting bulge is now considerably less concentrated ($r_{\rm PL} \approx 3''$–$5''$; the case $r_{\rm PL} = 4''$ is displayed in Fig. 2*b*), and the disk distribution is smoothly increasing also near the center. The resulting rotation curve is insensitive to the assumed mass-to-luminosity ratio of the unresolved central source, at least if it is $M/L_H < 0.1$. The most important difference as compared with the model of Figure 2*a* is that the overall rotation curve (Fig. 3*b*) is now fairly well consistent with a radius-independent M/L_H throughout the system, with $M/L_H \approx 0.75$ for both the bulge and disk regions. The rotation curve is also fairly insensitive to the details of the bulge/disk decomposition: for example, if $r_{\rm PL}$ is varied between 3″–5″, with a corresponding change in the fitted disk component, the combined rotation curve differs less than 5% from that of Figure 3*b*. This interval in bulge scale length corresponds to $M_{\rm bulge}/M_{\rm disk} = 0.11$–$0.37$.

There are several local deviations between the observed azimuthally averaged rotation curve and that following from the luminosity distribution for a constant M/L_H. The most prominent are the bump near 10″ and the depression between $r = 10''$–$35''$. In principle, this might simply indicate a significant M/L_H gradient (between the bulge/disk and within the disk). For example, allowing $(M/L_H)_{\rm bulge}$ to exceed $(M/L_H)_{\rm disk}$ would work in the direction of producing the bump near 10″. However, the depression between 15″ and 35″ would be harder to reproduce, as the disk curve has its maximum near 30″. We will demonstrate later that these features (especially the bump near 10″) of the rotation curve can be accounted for by the modest noncircular motions associated with the weakly barred potential, without additional assumptions of M/L_H. This is not surprising: for example, Duval & Athanassoula (1983) have shown that the axisymmetric rotation curve can be very strongly distorted in the case of strong bars.

4.2. *Resonance Locations*

In the limit of infinitesimal perturbations, the main resonance locations can be estimated from the rotation curve with the help of the epicyclic approximation. The corotation resonance corresponds to $\Omega(r) = \Omega_{\rm bar}$, where $\Omega(r)$ is the angular speed and $\Omega_{\rm bar}$ is the pattern speed of the bar. Inner and outer Lindblad resonances correspond to $\Omega \pm \kappa/m = \Omega_{\rm bar}$, with $m = 2$, where κ is the epicyclic frequency of radial oscillations; a minus sign corresponds to inner resonances. Similarly, $m > 2$ corresponds to so-called ultraharmonic resonances. In the case of finite perturbation amplitude, resonance locations shift as the characteristic angular and radial frequencies differ from the epicyclic values, but these relations are still useful as first approximations. In what follows we often refer to ILR, OLR, etc., radii without each time reminding that they are accurate only in the limit of the epicyclic approximation.

Some limits for the pattern speed of IC 4214 can now be immediately set by comparing the morphology and the rotation curve. Figure 4 displays the $\Omega \pm \kappa/m$ curves for $m = 2$, 4 resonances, arising both from the observed rotation curve and from the model of Figure 3*b*. For example, the bar must end inside the corotation resonance, because beyond this radius there are no orbits that can support the bar. As a lower limit for the corotation radius, we can use the major axis of the inner ring in the deprojected image (Paper I). This gives $r_{\rm cr} > 28''$ and an upper limit estimate of $\Omega_{\rm bar} < 55$ km s^{-1} kpc^{-1}. Similarly, if the outer ring at $r \approx 65''$ is connected with the OLR, this indicates $\Omega_{\rm bar} \approx$ 30–35 km s^{-1} kpc^{-1}. In Paper I a nuclear ring feature was identified at $r \approx 7''$. For the model rotation curve of Figure 3*b* this would correspond to the ILR if $\Omega_{\rm bar} \approx 60$ km s^{-1} kpc^{-1}. However, for the case of a noninfinitesimal perturbation, the epicyclic approximation is most likely to fail at the ILR: the true location of the resonance in terms of the transition between various orbital families can be shifted considerably inward (see § 5), reducing the actual $\Omega_{\rm bar}$ corresponding to a given ILR distance.

4.3. *Nonaxisymmetric Potential*

The radial behavior of various nonaxisymmetric density components in the *H*-band image resembles what is seen in the *I*-band very well (Saraiva 1997) and is not displayed here. Figure 5 displays the Fourier amplitudes of the nonaxisymmetric gravitational potential. Compared with the dominant $m = 2$ component, the other even components are much weaker. In terms of amplitudes of tangential forces F_T, the maximum of $F_{Tm=4}/F_{Tm=2} \approx 0.3$ at $r \approx 33''$, just beyond the inner ring region. On the other hand, the maximum of $F_{Tm=2}/F_{Tm=0} \approx 0.14$ at $r \approx 26''$. The $m = 1$ component, although much larger than the other odd components, or even the $m = 4$ component, is probably not significant, as it is very sensitive to the centering of the image.

In most of our simulations we decided to smooth the amplitude in the inner portions, by forcing the $m > 0$ density amplitudes to fall linearly to zero inside $r = 20''$. Also, the phase of the density components is forced into a

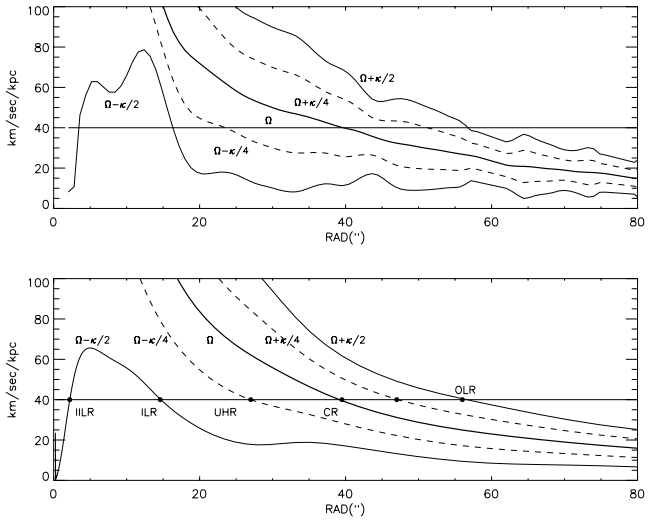

FIG. 4.—The curves Ω, $\Omega \pm \kappa/2$, and $\Omega \pm \kappa/4$, where Ω and κ stand for angular and epicyclic frequency, respectively. The upper frame corresponds to the observed azimuthally averaged Hα rotation curve, whereas the lower frame corresponds to the rotation curve of Fig. 2*b* with $M/L_H = 0.75$. The main resonances as calculated from the epicyclic approximation are indicated in the lower frame for the pattern speed $\Omega_{\rm bar} = 40$ km s^{-1} kpc^{-1}; the same horizontal line is shown in the upper frame as well. A distance of 31.6 Mpc has been assumed for IC 4214.

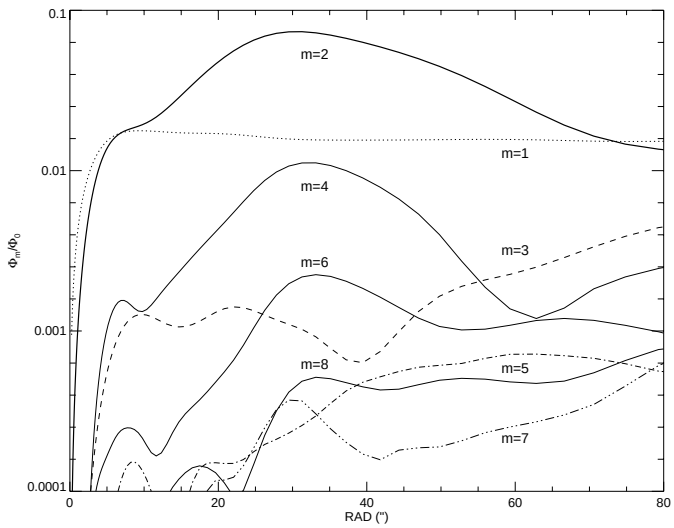

FIG. 5.—The Fourier components of the disk gravitational potential derived from *H*-band data. The bulge + nuclear source model of Fig. 2*b* has been subtracted, and the assumed orientation for the disk is $i = 52°$ and $\phi = 170°$. Amplitudes of nonaxisymmetric components are scaled by the disk's axisymmetric $m = 0$ potential.

constant value for $r < 30''$. This eliminates the effects of the nonaxisymmetry of the innermost regions, which might reflect changes in M/L_H rather than density variations. Also, this suppresses any artificial nonaxisymmetry produced by possible errors in disk/bulge decomposition and deprojection. However, we also performed runs with the gravitational field following from the raw density components, thus retaining the $\approx 30^\circ$ deviation in the phase of the potential minimum in the innermost region with respect to the bar direction.

As noted earlier, the uncertainty in the true orientation of IC 4214 impacts the magnitude of the nonaxisymmetric part of the potential (Fig. 6). Since the bar major axis is close to the nodal line of the galaxy, a smaller (larger) assumed inclination strengthens (weakens) the amplitude of the nonaxisymmetric deformations. Altogether, the about 10° uncertainty in inclination implies about 10% uncertainty in the maximum amplitude of the nonaxisymmetric gravitational field. However, this holds only in the bar region: near the outer ring the amplitude is sensitive also to the assumed ϕ, and the amplitude varies within a factor of 2 for the various orientations.

The other important source of uncertainty in the amplitude of nonaxisymmetric perturbations is the unknown vertical structure. Figure 6*b* displays the gravitational potential in the case the vertical structure is assumed to follow a Gaussian distribution $\rho(r, z) \propto \sigma_0(r) \times \exp[-1/2(z^2/z_0^2)]$, with z_0 in the range of $1''.25$–$10''$. The maximum of the $m = 2$ potential component is reduced by about 35% for this thickness interval. This is consistent with Quillen (1996), who found that doubling the scale height typically leads to a 10%–15% reduction in the potential amplitude, and also that different vertical profiles lead to practically identical results for the same scale height z_0. However, for the outermost disk ($r > 60''$) the potential amplitude is practically independent of z_0. This is because the nonaxisymmetric potential in this region is dominated by the bar and the smoothing of the gravitational potential due to the vertical thickness is ineffective on radial scales $\gg z_0$.

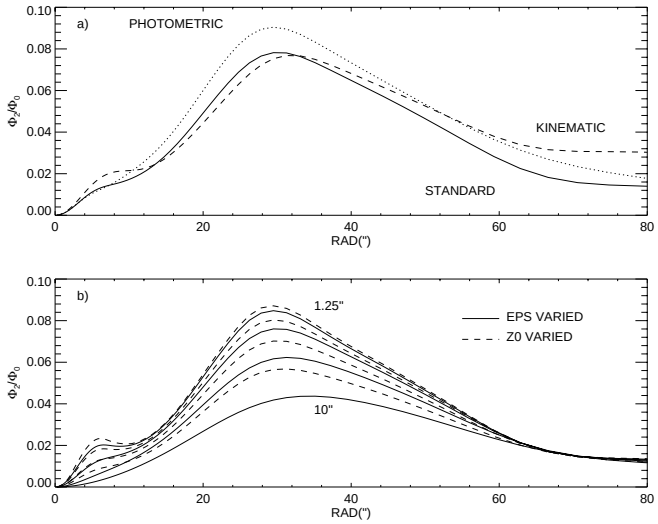

FIG. 6.—(*a*) The influence of the assumed IC 4214 orientation on the amplitude of the $m = 2$ potential (measured relative to the $m = 0$ component). The solid line refers to the standard orientation adopted in simulations, $(\phi, i) = (170^\circ, 52^\circ)$, whereas the dashed and dotted lines refer to the kinematic orientation $(169^\circ, 57^\circ)$, and the photometric orientation $(175^\circ, 47^\circ)$ as derived in Paper I, respectively. In (*b*) the effects of a nonzero vertical thickness are compared with that due to softened gravity for a two-dimensional density distribution. The vertical profile was modeled with a Gaussian profile, with vertical scale length $z_0 = 1''.25$, $2''.5$, $5''.0$, and $10''$ (*dashed lines, top to bottom*). Solid lines indicate corresponding amplitudes for a two-dimensional disk with the same values assigned to ϵ.

Studies of edge-on galaxies at optical wavelengths yield typically $z_0/r_e \approx 1/6$ (van der Kruit & Searle 1982), whereas near-IR measurements favor thinner disks with $z_0/r_e \approx 1/12$ (Barnaby & Thronson 1992; Rice et al. 1996). For IC 4214 with $r_e \approx 20''$, the IR measurements would thus suggest $z_0 \approx 1''.5$. However, some three-dimensional simulations (e.g., Raha et al. 1991) show significant vertical evolution of the bar, i.e., formation of a boxy bulge. This means that bars can be quite thick, so that in the bar region the most appropriate z_0 might be even a factor of 2–4 larger than for the disk. To account for this possibility, we adopt $z_0 = 3''.3$ as our nominal value for the bar region (or $z_0/r_e \approx 1/6$). The overall amplitudes are practically unaffected if the same z_0 is adopted throughout the disk. Thus we found it unnecessary to use two separate scale heights as Lindblad et al. (1996) did.

Figure 6*b* compares also the amplitudes with strictly two-dimensional distributions, but with gravity softening ϵ having the same values as given above for z_0. For small ϵ the correspondence between ϵ and z_0 is good, whereas with increased ϵ softening suppresses the gravitational field too efficiently. Our standard value in simulations, $\epsilon = 2''.5$, corresponds very closely to $z_0 = 3''.3$. We also perform simulations with $\epsilon = 5''$, corresponding to $z_0 \approx 9''$, thus mimicking a truly "thick" bar. The difference between these two models corresponds to $\approx 20\%$ reduction in the amplitude of the nonaxisymmetric bar perturbation.

The axisymmetric forces are also affected by the nonzero vertical thickness, although less than the amplitude of nonaxisymmetric force. The reduction of radial forces was already illustrated in Figure 3*b*, where the velocity curves corresponding to both $\epsilon = 2''.5$ and $5''$ were displayed (the relation between z_0 and ϵ holds also for axisymmetric forces). The thickness correction is quite small, and corresponds to a slightly modified M/L_H ratio.

5. SIMULATIONS

We now turn to simulations, performed with the above determined potential. Based on the estimates of § 4, we use $\Omega_{\rm bar} = 40$ km s^{-1} kpc^{-1} as a first guess for the bar pattern speed. This places corotation at $r \approx 39''$, or slightly outside the major axis of the inner ring (at $r \approx 28''$). The gravitational softening is $\epsilon = 2''.5$, corresponding to $z_0/r_e \approx 1/6$. The disk orientation is fixed to $(\phi, i) = (170^\circ, 52^\circ)$. The main parameters affecting the morphology and kinematics are the bar amplitude and pattern speed. Both these factors are studied separately.

5.1. *Bar Amplitude*

Figure 7 compares the gas morphology in simulations with the Hα and *B*-band images of IC 4214. Besides the nominal strength of the nonaxisymmetric potential derived in § 4, Figure 7 also studies simulations where the bar amplitude has been reduced, or slightly increased, by a constant factor A for all radii. The range $A = 0.1$–1.15 is studied, and in each case the axisymmetric potential is kept fixed. A small change of A from unity could be interpreted as a thickness effect: $A = 1.15$ corresponds roughly to $z_0/r_e = 1/12$ and $A = 0.75$ to $z_0/r_e = 1/2$. A larger reduction

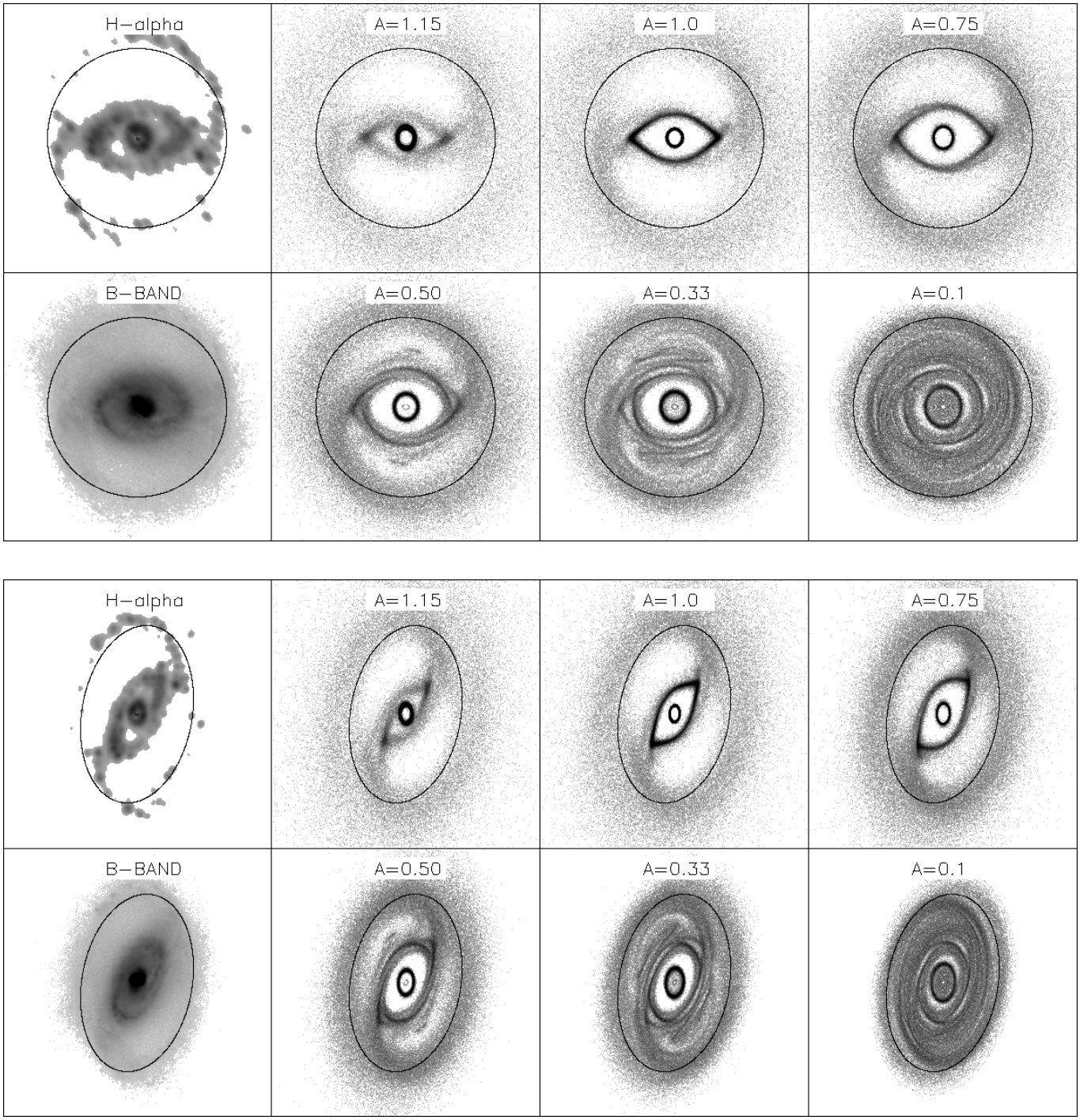

FIG. 7.—The gas morphology in simulations with different bar amplitudes A. In each case $\Omega_{\rm bar} = 40$ km s^{-1} kpc^{-1}. To improve the resolution of the density plots, snapshots at 10 different instants of time have been superposed, on a coordinate system corotating with the bar potential. The snapshots correspond to five to 12 bar rotations (about 0.8–1.8 Gyr) since the beginning of the run. The thickening of the nuclear ring for $A = 1.0$, and especially for $A = 1.15$, results from this superposition (see Fig. 13 legend for more explanations). Density plots displayed in subsequent figures are obtained in a similar manner. In (*b*) the projection on the sky is shown, with nominal orientation parameters $(\phi, i) = (170°, 52°)$. To aid comparisons, a circle in the plane of the disk, with a radius of 60″, is shown in each frame. The initial gas cloud distribution was uniform inside $r = 60''$, with a smooth transition to zero between $r = 60''$ and 80″. In each case the frame size is $90'' \times 90''$.

from unity would require (1) the M/L_H ratio of the disk (but not that of the bulge) to be in fact smaller than anticipated above ($M/L_H = A \times 0.75$), and (2) that IC 4214 has an additional dark halo component that would account for the amplitude of the rotation curve [$M_{\rm disk}/M_{\rm halo} \approx A/(1 - A)$]. Moreover, the shape of the rotation curve of the halo should be close to that of the disk. The advantage in using A as a free variable (instead of z_0/r_e or M/L_H or exact orientation) is that various comparisons are more accurate as the model rotation curve and resonance distances (as calculated from the epicyclic approximation) stay fixed.

Several effects of varied bar amplitude are readily discerned from Figure 7. Near the nominal amplitude $A = 1$ the inner ring is a very peaked or pointed oval, whereas as

the amplitude decreases the ellipticity of the ring decreases, it becomes less pointed, and its structure starts to divide into several distinct braids. Even further reduction of the amplitude ($A = 0.1$) transforms the ring into four distinct arm segments, providing a clear illustration of the connection between the UHR and the inner ring. For $A = 1.15$ the inner ring has nearly vanished. The size and shape of the nuclear ring is also strongly dependent on amplitude. As A increases, the nuclear ring shrinks and gets more and more elongated, in accordance with previous results (van Albada & Sanders 1982). For $A = 1$, the semimajor axis of the nuclear ring is only about 50% of that calculated from the epicyclic approximation ($A = 0$). Weak signs of an inner ILR are also visible in some runs. Finally, the size of the outer spirals increases with increasing A and the region around the Lagrangian points L_4 and L_5 is more efficiently cleared. Table 1 collects the ring distances and shapes measured from these simulations. Note, however, that the measurements are fairly subjective, especially for the inner ring if A is close to 0.5, because several arm segments are present. For this reason a range of semimajor and semiminor distances is given for the features associated with the inner ring region.

The best resemblance to IC 4214's morphology in the B-band, with a fairly smoothly curving inner ring with some spiral segments, is obtained for $A \approx 0.5$. For smaller A the braiding is clearly too strong. However, for $A = 0.75$ or 1.0 the inner ring is very reminiscent of the Hα morphology, with a much more peaked appearance (see also the $U-I$ image in Fig. 7 in Paper I). In what follows we concentrate on the comparison of simulated gas with Hα observations. $A > 1$ can be ruled out based on the disappearance of the inner ring. The overall correspondence for sizes of the simulated rings is best for $A \approx 0.75$ (see Table 1). The most evident defect of all of the models is the lack of spirals between the inner and the nuclear ring. Also, the nuclear ring is more distinct than in IC 4214 and has a different orientation than the observed nuclear ring or the central oval of the galaxy.

The above morphological features have clear kinematic counterparts. Figure 8 compares the simulated and observed Hα zero-velocity line, which is sensitive to the bar-induced radial velocities. For example, the nuclear ring exhibits a distinct shift in the zero-velocity line, in agreement with observations. A bend in the same direction is also seen at the outer ring, moving gradually inward with respect to ring location as A is increased. The inner ring region shows wiggles in the zero-velocity line, associated with the spiral segments. A similar connection between a spiral segment and a detail in the observed velocity field is visible at the western side (at $r \approx 25''$). The variations of the zero-velocity line with A are quite small in the inner regions, whereas for the outer ring the shift scales with A: best agreement is again seen for $A \approx 0.75$.

The corresponding ring-related features are also seen in the major-axis rotation curve, which is affected by the bar-induced tangential velocities. Figure 9 displays both the velocity cut along the major axis (for gas particles) and the azimuthally averaged velocity curves calculated with the Warner, Wright, & Baldwin (1973) method. As the data for simulated gas particles contain large gaps as a result of the concentration of particles on rings, we have also constructed the averaged velocity curve using test particle stars. For large A the inner ring appears as a single bump in the major-axis cut but shows clear resonance signature as A is decreased. Similar deviations from the circular velocity curve are seen in the outer ring region. Application of the Warner et al. method to test particle stars shows a strong drop outside the nuclear ring region at $r \approx 10''$–$25''$. In the same region the curve for gas particles shows a small upward bend, but this corresponds to very few particles. It is tempting to associate this downward bend (see especially $A = 0.75$ and 1.0 cases) for test particle stars with the similar bend in the observed curve.

The correspondence between kinematic features seen in Figures 8 and 9 and major resonances becomes especially clear in Figure 10*a*, comparing the velocity curve in a low bar amplitude simulation ($A = 0.1$) with that obtained from a linear approximation ignoring viscosity. We have applied the Binney & Tremaine (1987, p. 146) treatment of weakly perturbed closed loop orbits and used the same gravitational potential (with $m = 0$, 2, and 4 terms included) as in the simulations. The calculated directions of major-axis velocity shifts around various resonance locations agree well with the simulated kinematic features. Not surprisingly, near exact resonances the linear treatment fails, as it predicts singular behavior and abrupt 90° changes in orientation of orbits. The former problem would be removed by a more accurate treatment of resonance orbits (Binney & Tremaine 1987, p. 151), whereas the introduction

TABLE 1

SIZES OF SIMULATED RINGS

A	a_{NR} (arcsec)	q_{NR}	a_{IR} (arcsec)	b_{IR} (arcsec)	a_{OR} (arcsec)	q_{OR}
0.01	15.0	1.0	28	28	60	0.95
0.10	13.4	0.9	27–29	24–26	61	0.87
0.33	10.3	0.9	28–36	21–28	61	0.82
0.50	8.8	0.91	29–36	19–26	63	0.83
0.75	7.3	0.87	27–31	19–22	65	0.83
1.00	6.1	0.84	24–29	15–16	70	0.77
1.15	5.8	0.81	20–27	14–15	73	0.72
OBS.....	7.0	0.84	28	22	64	0.83

NOTE.—a and q stand for semimajor axis radius and axis ratio of simulated nuclear ring (NR) and outer ring (OR) structures. For the inner ring (IR), the ranges of semimajor and semiminor axis radii (b) are given, as explained in the text. OBS stands for values deduced in Paper I: for NR from Hα, and for IR and OR from B-band observations. A is the dimensionless bar amplitude.

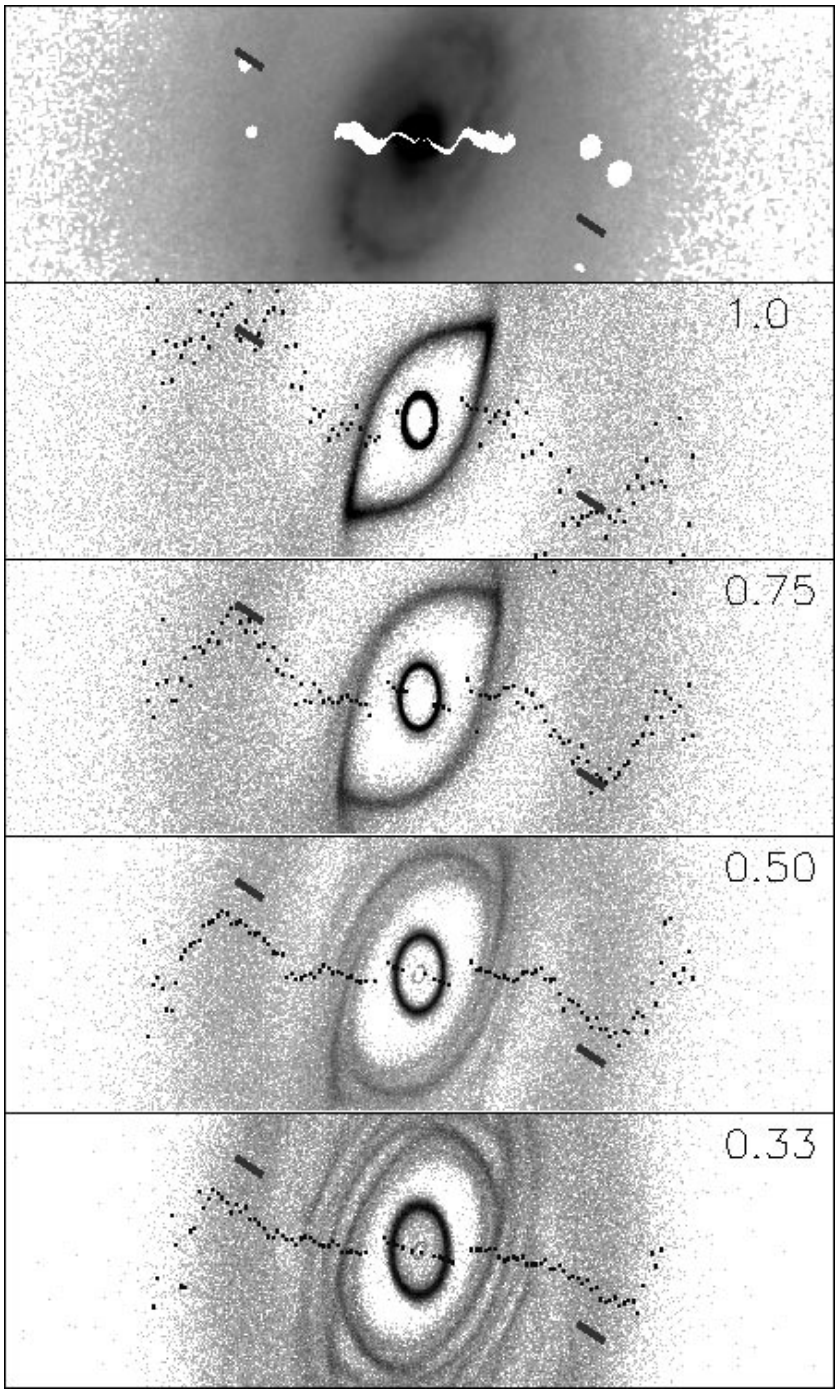

FIG. 8.—Zero-velocity lines in simulations of Fig. 7, for $A = 1.0$–0.33. The uppermost frame displays the observed Hα zero-velocity line, overlaid on a *B*-band image. In the continuous inner region, velocities within ± 10 km s^{-1} from the systematic velocity are shown, whereas for the outer parts velocities within ± 40 km s^{-1} are displayed. Note that the actual zero-velocity line in the outer parts (*thick black lines*) goes south of the two blobs in the west. The size of each frame is $180'' \times 60''$. In the simulation plots the zero-velocity line has been constructed from particles within ± 10 km s^{-1} of the systematic velocity: their vertical locations have been averaged in $1''$ wide zones.

of viscosity leads to a continuous change of orientation across the resonance (see, e.g., Hänninen & Salo 1994, addressing collisional behavior in the context of satellite resonances in planetary rings). In any case, the linear approximation provides a clear association of the inner ring velocity shifts with that in the UHR. Note that there is no sign of the corotation resonance in simulation kinematics. This is exactly as predicted by the linear treatment. Similarly, the zero-velocity curve from linear approximations agrees with that in the low-amplitude simulation (Fig. 10*b*). Again, the corotation location does not show any special behavior.

The advantage of comparing one-dimensional velocity cuts (zero-velocity line, major-axis rotation curve) is the easy comparison between various simulations. However, Figure 11 demonstrates the good overall agreement between the simulated two-dimensional velocity field versus Hα observations, for $A = 0.75$. As the gas velocity field con-

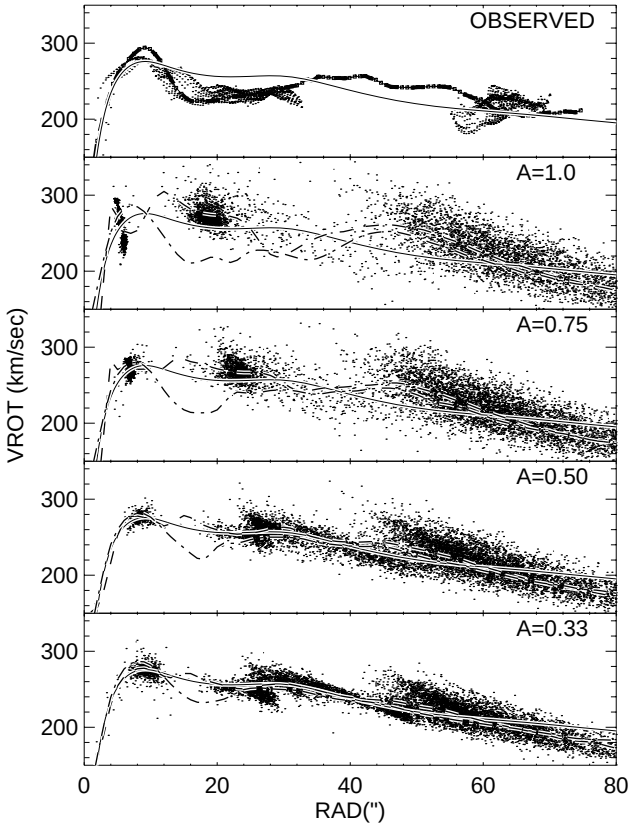

FIG. 9.—Major-axis rotation curves in the simulations of Fig. 7. The points stand for individual particles within 5° of the major axis ($\phi = 170°$), and the solid line indicates the circular velocity curve calculated from the axisymmetric potential. The dashed and dash-dotted curves display the azimuthally averaged rotation curves derived with the Warner et al. (1973) method (with ϕ fixed to 170°), calculated for gas and stellar test particles, respectively. The initial velocity dispersion of stellar test particles was 10% of the circular velocity. The uppermost frame displays the observed major-axis cut (*points*), and the thick symbols denote the azimuthally averaged rotation curve.

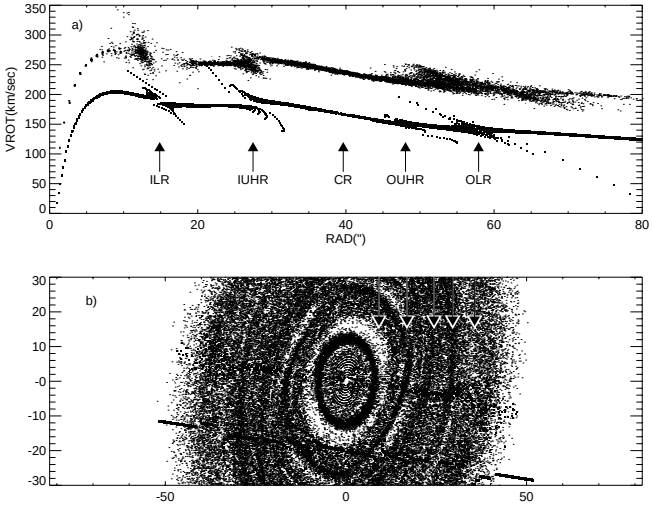

FIG. 10.—Comparison of the kinematics obtained in the low-amplitude run ($A = 0.1$) with that calculated from the linear approximation of closed loop orbits (Binney & Tremaine 1987, p. 146). In (*a*) the major-axis rotation curve is shown, whereas (*b*) compares the zero-velocity line (analytical curves are superposed with downward shifts). Major-axis velocities are affected by the tangential streaming velocity $V_{\rm tan}$ owing to the bar, whereas the zero-velocity line is mainly sensitive to the radial velocity $V_{\rm rad}$. In the upper frame the main resonance locations are indicated by arrows; the labels "IUHR" and "OUHR" stand for inner and outer $m = 4$ UHRs, respectively. In the lower frame the arrows indicate the same resonance locations. In the linear approximation, $V_{\rm rad} \propto -mC(\Omega - \Omega_{\rm bar})$ sin $m\theta$, where θ denotes the angle from the potential minimum (bar major axis) and C is the amplitude, changing sign at each Lindblad resonance and at the CR resonance (C is positive outside OLR). The main term of $V_{\rm tan} \propto -C\Omega$ cos $m\theta$.

tains large gaps owing to the concentration of particles on rings, the velocity field of test particle stars is also shown, covering the whole disk region.

5.2. *Bar Pattern Speed*

The above comparisons show quite good agreement between the $A = 0.75$ model and observations. To check the influence of the bar pattern speed, Figure 12 compares the morphology in runs with $\Omega_{\rm bar} = 35$–50 km s^{-1} kpc^{-1}. Besides the $A = 0.75$ case, simulations with $A = 0.5$ are also shown.

As can be expected, increasing $\Omega_{\rm bar}$ reduces the scale of rings since all resonance distances move inward. For $\Omega_{\rm bar} = 50$ km s^{-1} kpc^{-1} and $A = 0.75$, the nuclear ring has shrunk dramatically, becoming very elongated in the direction of the bar major axis. For increased $\Omega_{\rm bar}$ the inner ring develops a double structure, whereas for $\Omega_{\rm bar} = 35$ km s^{-1} kpc^{-1} several spiral segments strengthen the braided appearance. In general, an increase (reduction) in $\Omega_{\rm bar}$ affects the morphology in roughly the same manner as increased (reduced) bar amplitude. The same tendency was confirmed in kinematic comparisons similar to Figures 8 and 9. Thus, for example (see Fig. 12*b*), the $\Omega_{\rm bar} = 45$ km s^{-1} kpc^{-1}, $A = 0.5$ case resembles the $\Omega_{\rm bar} = 40$ km s^{-1} kpc^{-1}, $A = 0.75$ case. Similarly, for $\Omega_{\rm bar} = 35$ km s^{-1} kpc^{-1} a good match can be obtained for $A = 1$.

For increased $\Omega_{\rm bar}$ the models of Figure 12 show features that are not present in IC 4214, namely, gas concentrations near Lagrangian points L_4 and L_5 (the area of banana orbits; Contopoulos & Grosbøl 1989). Nevertheless, for the studied potential (for $A > 0.1$), L_4 and L_5 are unstable, so that these regions must eventually clear out: gradual clearing was also observed in simulations.

The overall correspondence between simulations and observations seems acceptable when $\Omega_{\rm bar} \approx 35$–$45$ km s^{-1} kpc^{-1}, with A close to 0.75. This interval places the corotation at $39'' \pm 3''$, a bit outside the end of the bar. If $r_{\rm bar}$ is identified with the major axis of the inner ring ($\approx 28''$), this yields $r_{\rm bar}/r_{\rm cr} \approx 0.67$–$0.77$. This conforms to the common trend in early-type galaxies (Elmegreen & Elmegreen 1995; Elmegreen 1996).

5.3. *Dissipation*

Because of dissipative impacts, gas clouds tend to synchronize their velocities, which gradually drives clouds toward closed, nonintersecting periodic orbits. As mentioned in § 3, the general features of the simulated gas population are fairly insensitive to the cloud parameters. However, some characteristics do depend on impact frequency ω_c, which must be kept in mind in comparison of simulated morphology with observed. Figure 13 displays examples of simulations with different impact frequencies in the $A = 0.5$ case, achieved by varying the gas cloud radius in the range 0.1–10 times the nominal value. Collision frequencies in various ring zones are collected in Table 2. The

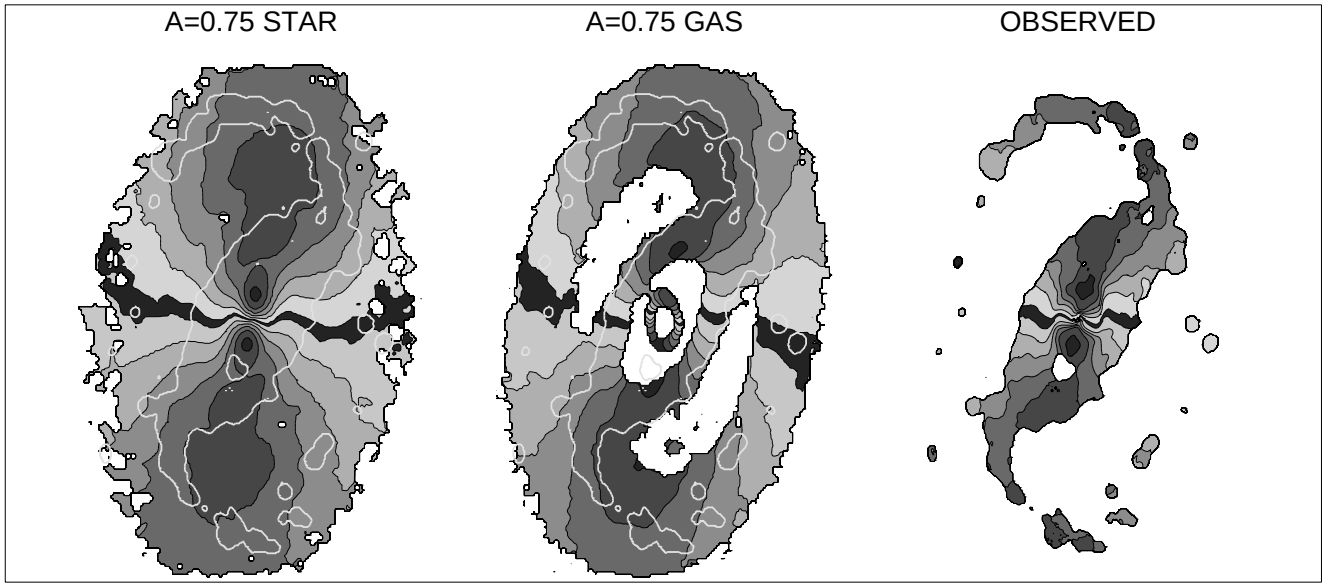

FIG. 11.—Two-dimensional velocity field of the best model ($\Omega_{bar} = 40$ km s^{-1} kpc^{-1}, $A = 0.75$), compared with observations. The interval between contours is 40 km s^{-1}, except for the middle contours, which correspond to ± 10 km s^{-1}.

same morphological features exist in all simulations: however, the sharpness of the rings and spirals rises with ω_c as expected. The same is true for kinematic signatures. The clearest difference is the orientation of the outer ring, which becomes distinctly trailing in the high-viscosity case. Also, for high ω_c, clumps appear in the outer ring.

5.4. *Miscellaneous Experiments*

The importance of higher order components of the nonaxisymmetric potential was tested in simulations retaining only the $m = 2$ component. The overall features were much the same, but differences could be seen in smaller scale details like the shape of the inner ring, which loses its braided appearance and becomes more diamond shaped for $A = 0.5$ when only $m = 2$ terms are included. The connection of the inner ring to the UHR as a result of nonlinear effects is still evident, although the perturbation itself does not contain $m = 2$ terms. Even for $A = 0.1$ the inner ring can be discerned, although it becomes much weaker than in the presence of $m = 4$ terms. With inclusion of both $m = 2$ and $m = 4$ components, practically all features of previous models are retained. We also checked the influence of the density smoothing we have adopted (see § 4): the simulation with the potential calculated from the nonsmoothed density distribution for $r < 20''$ is indistinguishable from the standard one, except that the inner nuclear ring is stronger: its orientation has also changed from that aligned with the bar by about 30°, thus becoming aligned with the local direction of the potential minimum near the center.

TABLE 2

IMPACT FREQUENCY ω_c IN SIMULATIONS OF FIGURE 13

	CLOUD SIZE		
ZONE	$0.1 \times r_0$	r_0	$10 \times r_0$
Average	0.13	0.90	31
Nuclear ring.....	0.79	1.98	58
Inner ring	0.10	1.11	27
Outer ring	0.05	0.75	30

NOTE.—Units are impacts per particle per bar rotation period. Mean values over indicated regions correspond to values after about 10 bar rotations. The standard cloud size, 0.″005, is denoted by r_0.

Figure 14 displays the relative importance of the spiral potential on sustaining the observed outer spiral arms. This was tested by simulations in which the nonaxisymmetric density components outside the bar region were neglected (smooth truncation of the nonaxisymmetric density to zero between $r = 35''$–$40''$; "bar only" potential). Also shown are complementary simulations where only the nonaxisymmetric density beyond the bar region was included ("spiral only" potential). In the outer ring region the bar and spiral contributions to the total amplitude of the nonaxisymmetric potential are about the same, whereas the spiral contribution rapidly loses importance as we move inward. This accounts well for the behavior with $\Omega_{bar} = 40$ km s^{-1} kpc^{-1}: except for weaker outer spirals, the morphology is almost unaffected if the spiral contribution is omitted. In the case of the "spiral only" potential, the outer spirals resemble those with the "bar only" potential, but the inner ring is much rounder and the nuclear ring is clearly larger as expected for the weak perturbation.

Somewhat surprising is the very different behavior for $\Omega_{bar} = 30$ km s^{-1} kpc^{-1}: the "bar only" potential cannot produce any outer spirals and even the inner ring is very weak. Compared with $\Omega_{bar} = 40$ km s^{-1} kpc^{-1}, this can be explained by the fact that the main resonances have moved outward and the inner ring thus is situated in a region of weaker nonaxisymmetric potential. However, the response to the spiral potential is strong also in the $\Omega_{bar} = 30$ km s^{-1} kpc^{-1} case, although the nonaxisymmetric potential amplitude in the region of the inner ring is comparable to the "bar only" case. Because of the spiral twist of the potential, the forces are larger in the spiral case. The strong dependence of the strength of the outer spirals on the bar pattern speed might explain why some previous simulations with

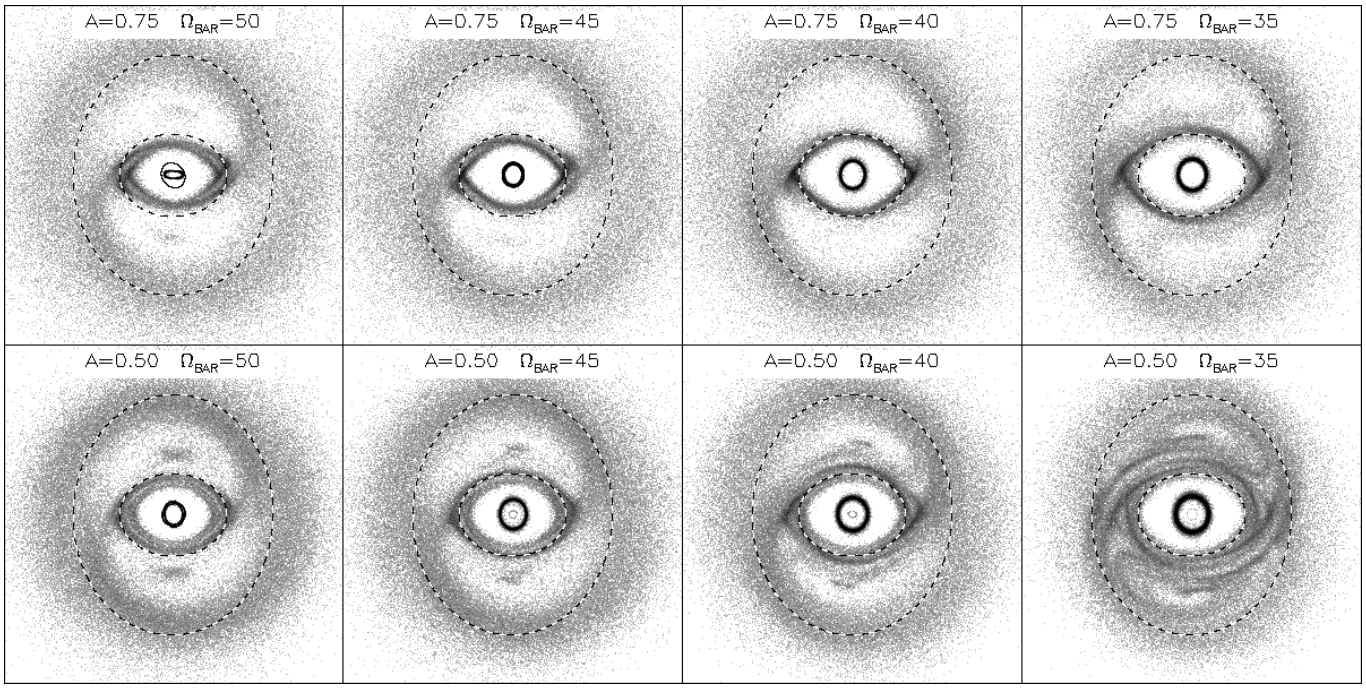

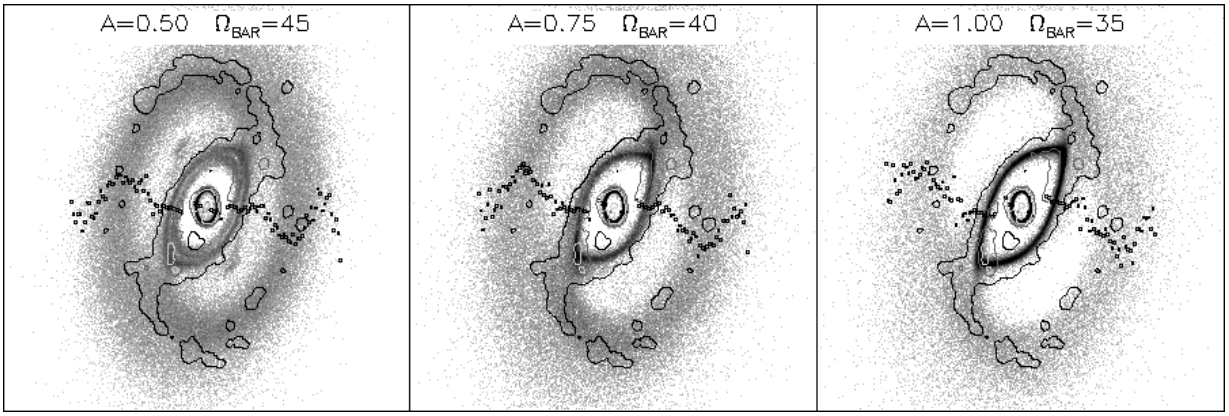

FIG. 12.—(*a*) Same as Fig. 7*a*, except that the gas morphology in simulations with different $\Omega_{\rm bar} = 35$–50 km s^{-1} kpc^{-1} is studied for $A = 0.5$ and 0.75. Dashed ellipses indicate deprojected fitted rings from observations (Paper I). For clarity, the observed nuclear ring is displayed only in the upper left frame. (*b*) Comparison of three different ($\Omega_{\rm bar}$, A) combinations leading to approximately similar morphology and kinematics. Symbols denote the simulated zero-velocity line, whereas contours trace the observed Hα distribution.

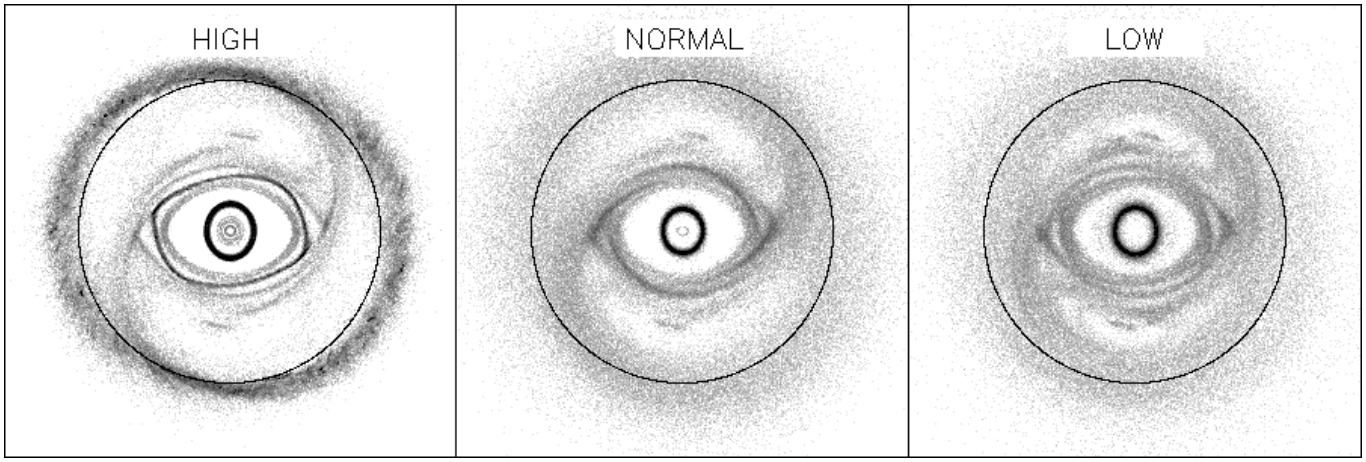

FIG. 13.—The influence of dissipation. In the first frame the cloud size is 10 times the standard value, the middle frame shows the standard case, and the last frame shows the simulation where the particle size is 0.1 times the standard. In each case $A = 0.5$ and $\Omega_{\rm bar} = 40$ km s^{-1} kpc^{-1}.

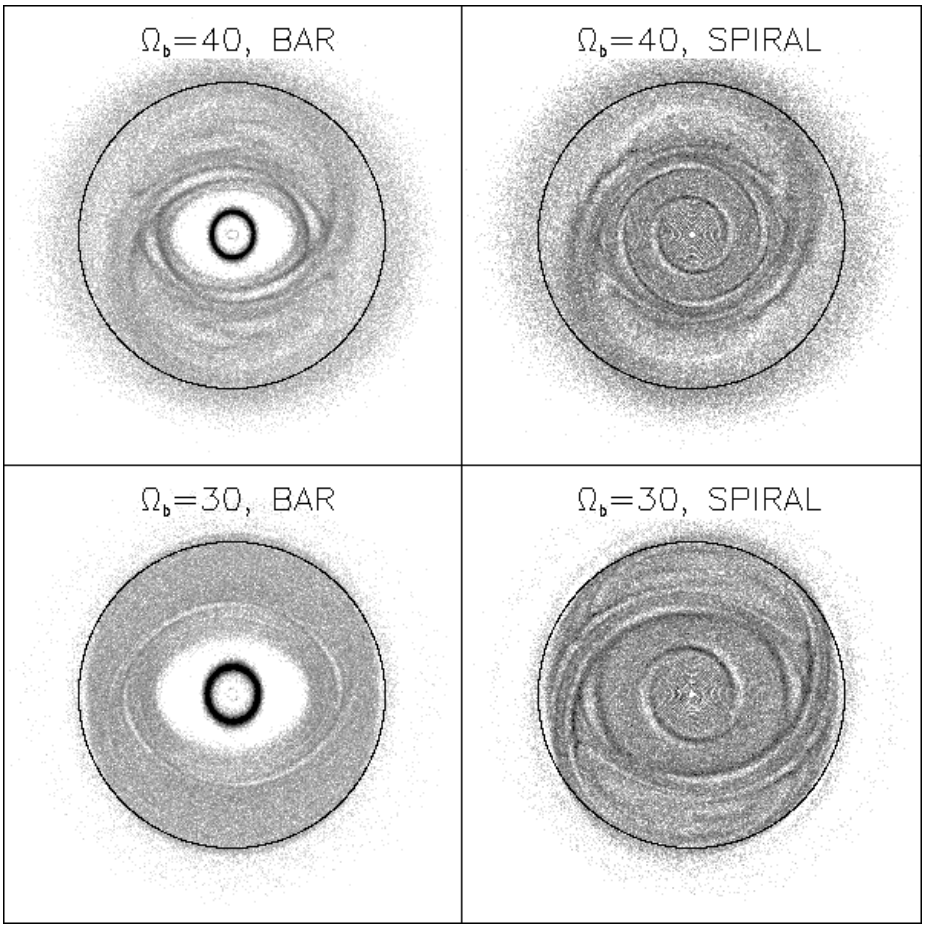

FIG. 14.—Effect of "bar" and "spiral" components on the morphology for $A = 0.5$, for $\Omega_{bar} = 40$ and 30 km s^{-1} kpc^{-1}. See text for the definitions of components.

"bar only" potentials (e.g., Hunter et al. 1988) could not produce significant spiral structure.

5.5. *Periodic Orbits*

Typical examples of periodic orbits in the regions of the inner and nuclear rings in two of our simulations are shown in Figure 15. The particle distribution is also plotted, to facilitate easy comparison between morphology and orbits. The orbits forming the nuclear rings belong to the x_2 family, being perpendicular to the bar (here we follow the notation introduced by Contopoulos; see, e.g., Contopoulos 1980; Contopoulos & Grosbøl 1989). The size of the nuclear ring depends on the bar strength, so that increasing its amplitude makes the ring smaller. When the perturbation is very small, the nuclear ring is exactly at the inner Lindblad resonance (outer ILR). With amplitude $A = 1.0$, its major axis is less than 50% of the resonance radius calculated from the epicyclic approximation. The reason for this behavior is the smaller region where x_2 orbits exist. Indeed, sometimes the inner Lindblad resonance is redefined as the radius inside which these orbits are stable (van Albada & Sanders 1982; Athanassoula 1992a). In some simulations with low A, another nuclear ring that is related to the inner ILR was seen: an example of a closed orbit contributing to this structure is also displayed in Figure 15.

In the high-amplitude case ($A = 1.0$), the structure of the inner ring is simple and can be explained by the x_1 orbits. In lower amplitudes the ring structure becomes more complicated and is formed by several tightly wound spiral arms. Several types of orbits, some even multiperiodic, are contributing to this shape. In general, they are less elongated than for large A. As mentioned above, simulations with very small perturbation show that the inner ring is related to the inner 4/1 resonance: in those simulations the ring appears as four extremely tightly wound spiral arms precisely at the resonance radius. Also, the twisted inner ring seen in the high-ω_c case of Figure 13 can be understood in terms of the orbital structure.

The outer pseudoring is in the vicinity of the outer Lindblad resonance. However, we could not find simple closed orbits in this area because of the presence of the spiral potential. When only the bar was included, the usual perpendicular and parallel orbit families appear. This is in accordance with the results of Contopoulos & Grosbøl (1989), who found that in the presence of both bar and spiral potentials, there are no closed orbits that can support the spiral between corotation and the outer 4/1 resonance.

The existence of collisions puts some limits on the orbits that the gas particles can follow so that they, for example, cannot stay in intersecting orbits. In simulations with a very strong bar ($A > 1$; see Fig. 7), the particles initially forming the inner ring are in such highly elongated orbits that they begin to cross some of the x_2 orbits. This is at least one of the processes that move particles from the inner to the

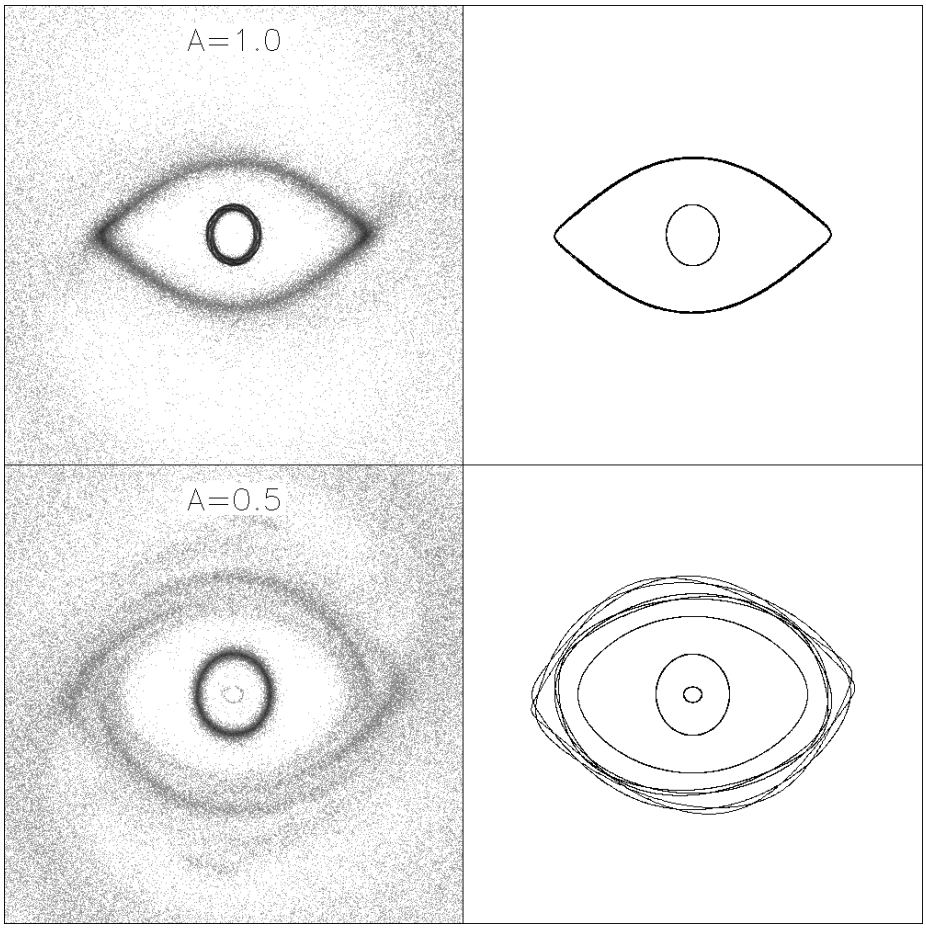

FIG. 15.—The upper two frames show the inner parts of the $A = 1$, $\Omega_{\rm bar} = 40$ km s^{-1} kpc^{-1} simulation (*left*) and some examples of closed periodic orbits contributing to the inner and nuclear rings (*right*). The lower two frames are the same for amplitude $A = 0.5$. An interesting detail visible in the upper left frame is the libration of the nuclear ring: as snapshots of several instants of time have been superposed, this manifests as a double structure in the plot (the same is seen also for $A = 1.15$ and 1.0 in Fig. 7). This libration might be an artifact related to the finite size of the simulation particles and the space available for the x_2 orbital family comprising the nuclear ring: in the case of libration, the particles cannot be confined into a closed orbit because of close-packing effects. However, they still move coherently, and the ring as a whole precesses with a common rate. Sometimes ($A \approx 1$ and large clouds) this leads to even $\pm 20°$ deviations around the mean direction. It is uncertain whether this could have any counterpart in real physical situations.

nuclear ring and apparently can lead to eventual disappearance of the inner ring.

Although we were mostly interested in orbits that are responsible for features seen in the gas morphology, we also found several multiperiodic orbits and orbits that are not symmetric with respect to either the major or the minor axis of the bar. Patsis, Athanassoula, & Quillen (1997) studied these kinds of orbits and their significance in the case of NGC 4314.

6. APPLICATION OF ORIENTATION METHODS ON SIMULATION DATA

As noted above, the IC 4214 orientation determined in Paper I by different methods disagrees considerably. The (ϕ, i) measured from outer isophotes was ($175° \pm 1\overset{\circ}{.}4$, $47° \pm 3°$), whereas the application of kinematic methods yielded ($169° \pm 1°$, $57° \pm 2°$). The presence of such a discrepancy is in itself easy to understand as the kinematic determination is certainly affected by the noncircular motions associated with the bar. Similarly, there is no guarantee that any of the isophotes of a barred galaxy are intrinsically circular. The mere morphological features in simulations performed with the above two (and some other) different orientations cannot clearly favor one over the other. However, we will show here that the observational difference in the results of these two methods becomes understandable if the same methods are applied to our IC 4214 simulation models. Moreover, simulations favor an intermediate, fairly well constrained orientation.

In the Warner et al. (1973) method, the galaxy is modeled as an axisymmetric disk with all matter on circular orbits. The minimization of velocity residuals between the observed velocity field and that obtained from this simplified model leads to a preferred set of orientation parameters and also gives the circular velocity curve. In the case of a barred galaxy, significant deviations from circular motions and axisymmetry are present, especially near the major resonances, and the deduced orientation thus differs from the true one. In order to see how large deviations (and to what direction) can be expected, we have applied the Warner et al. method to the simulations displayed in Figure 7, performed with different bar amplitudes. In each case the gas particle distribution and velocities were projected on the sky with the nominal orientation parameters (52°, 170°), and the global minimization of velocity residuals was performed. Differences between the "true" orientation (well

defined in the case of simulations) and that given by the Warner et al. method are displayed in Figure 16. Besides using the actual orientation of IC 4214's bar with respect to the nodal line, the whole range of $\phi_{\rm bar}$ values is explored, by rotating the simulation system in its plane by various angles before the sky projection.

According to Figure 16, the kinematic method tends to exaggerate the true inclination. For IC 4214's orientation ($\phi_{\rm bar} \approx 40°$), the deviation amounts to $\Delta i \approx 9°$ for $A = 0.75$. The somewhat surprising feature of Figure 16, namely, that the kinematic inclination is larger than the true one for all $\phi_{\rm bar}$, reflects the nonlinear behavior of perturbations. Indeed, if the Warner et al. method is applied to the velocity field resulting from the linearized loop orbit model mentioned in § 5, both positive and negative shifts in inclination are observed. This is also the case for the simulation with $A = 0.01$. However, even for such a small amplitude as $A = 0.1$, Δi is always positive with a maximum of about 3° when the bar is roughly parallel to the nodal line. The deduced position angle is less sensitive to the bar perturbation, and both negative and positive shifts are possible depending on the orientation. For $\phi_{\rm bar} = 40°$ the kinematic ϕ for $A > 0.5$ is about 1° smaller than the true one.

The measurement of outer isophotes in Paper I was made in the region $70'' < r < 90''$, just beyond the outer ring. This yielded a mean axial ratio of 0.698 over all filters used, corresponding to $i \approx 46°$ if thickness corrections are omitted. Now, the gas orbits with mean distance outside (inside) OLR are aligned along (perpendicular to) the bar. In the case of IC 4214, the predominance of outside or inside orbits could cause the inclination derived from isophotes to be either underestimated or overestimated, respectively. Because of nonlinear perturbations (inside and outside orbits can have a large overlap region), and because of viscous behavior of the gas (strong twists of gas streamlines), it is difficult to estimate beforehand the actual direction of net shifts in ϕ and i in a given region. We thus turn to the simulations. Instead of studying the simulated gas distributions, which had uniform initial distribution, we employ exponentially distributed test particle stars and compare their isophote behavior with respect to H-band data. This circumvents any problems in identifying the simulated gas particles with the observations. Also, instead of comparing the shape and orientation of isophotes in a single zone, the radial trends in ϕ and i are studied, enabling qualitative comparisons also with those simulations where the outer ring region falls to a slightly different location than in observations.

Figure 17 displays the behavior of stellar isophotes in the same simulations whose gas velocity fields were studied in Figure 16 with the kinematic method. The distribution of stellar test particles with $r_e = 20''$ mimics the radial distribution of IC 4214's disk, and the initial velocity dispersion assigned to them is 10% of the circular velocity at each

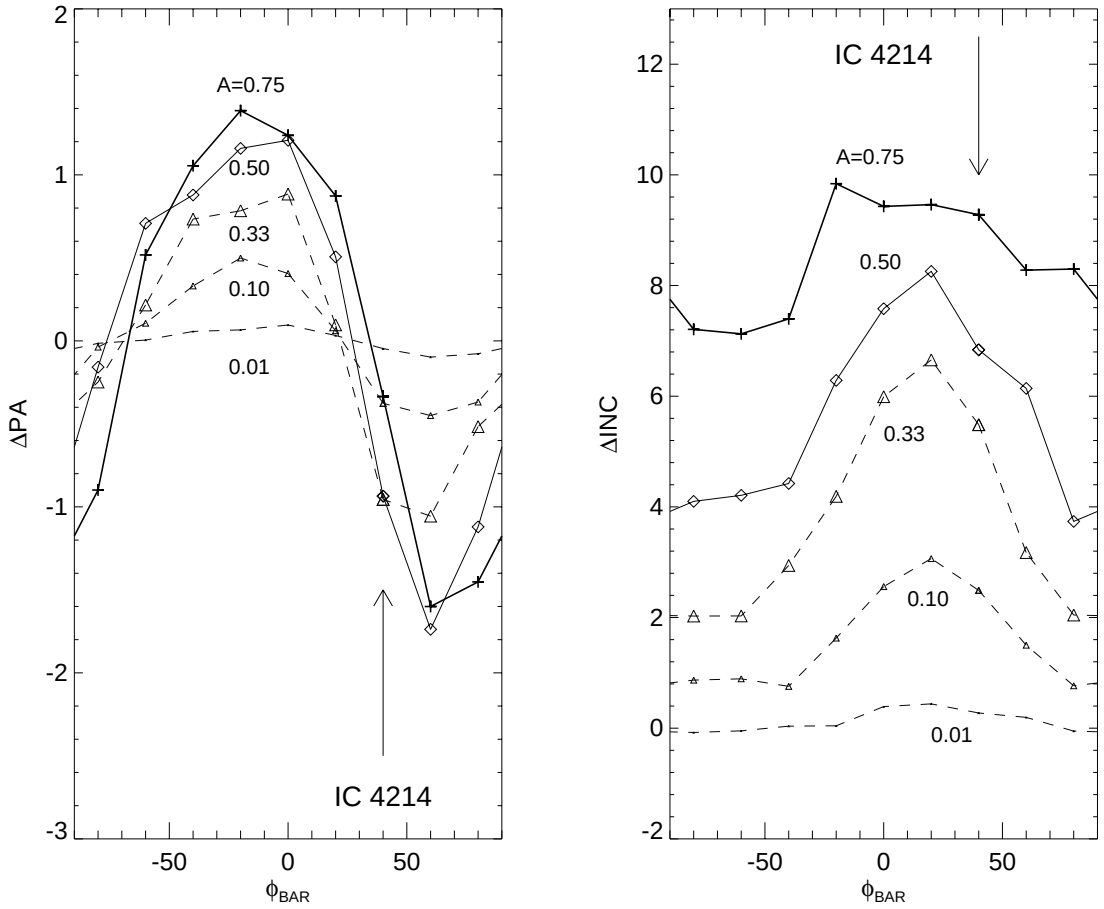

FIG. 16.—Application of the Warner et al. (1973) global minimization method to the simulations of Fig. 7. The deviations of derived kinematic orientation parameters from the actual orientation parameters $(\phi, i) = (170°, 52°)$ in simulations is shown as a function of $\phi_{\rm bar}$, the angle between the bar major axis and the galaxy nodal line. $\phi_{\rm bar}$ is measured along the disk plane in the direction of rotation. Arrows indicate the alignment of IC 4214's bar. Bar amplitudes in the range $A = 0.01$–0.75 are studied, while $\Omega_{\rm bar} = 40\ {\rm km\ s^{-1}\ kpc^{-1}}$.

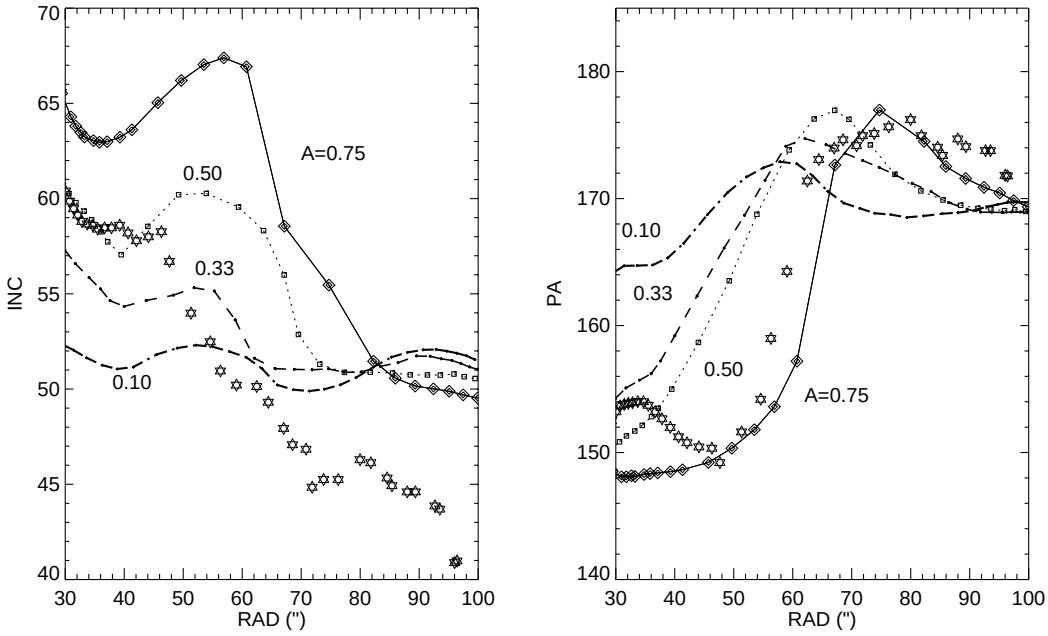

FIG. 17.—Behavior of stellar isophotes in simulations of Fig. 7. The stellar distribution is mimicked by noncolliding test particles with approximately the same initial radial profile as in IC 4214's disk ($r_e \approx 20''$). Asterisks denote the measured H-band isophotes (Paper I).

radius. For $A = 1.0$ the final velocity dispersion in simulations corresponds to Toomre parameter $Q_T \approx 1$ in the outer ring region (if we assume that all active mass is in the disk; correspondingly for $A = 0.5$, $Q_T \approx 2$). The test particle disk is strictly two-dimensional. However, we checked that the results are sensitive to neither the assumed velocity dispersion nor the vertical thickness of the simulation disk.

According to Figure 17, the outer ring region is associated with a large positive twist in ϕ and a strong reduction in i, in qualitative agreement with the H-band data. The strength of the bar affects both the amplitude of shifts and the radial location where they occur: an increase of A pushes the transition zone outward, in accordance with Figure 7 where the size of the outer spirals grew with stronger perturbation. In ϕ a fairly good match is obtained for $A \approx 0.75$, with $\phi \approx 175°$ at $r \approx 80''$. The same is true for the amplitude of the inclination shift, but the inclinations are systematically too large. Experiments with different Ω_{bar} near the nominal value yielded similar results. The only remedy we found to account for the observed axial ratio at $r \approx 80''$ was to change the nominal inclination we have so far assumed (52°) to 48°. With this modification the behavior of both ϕ and i is fairly well reproduced. An additional effect of using $i = 48°$ instead of $i = 52°$ is that because of the increased amplitude of the perturbation (see Fig. 6), the excess Δi obtained with Warner et al. method increases. The large kinematic inclination can thus still be accounted for in spite of the decreased nominal inclination.

However, the revised inclination has an effect on the angle of the outer ring with respect to the bar major axis: for $(\phi, i) = (170°, 48°)$ the outer ring *leads* by about 20° with respect to the perpendicular orientation. At first glance this seems improbable: for example, viscosity can only cause the outer ring to trail from the perpendicular orientation. However, the simulations of § 5 already present examples of such *apparent* leading twist; see, for example, the $\Omega_{bar} = 35$ km s^{-1} kpc^{-1} case in Figure 12. This is caused by the density asymmetry between the portion of the pseudoring where it starts from the bar and the back-winding region. A similar phenomenon might be seen in IC 4214, affecting the deprojected outlook. Altogether, the influence on the total potential is insignificant, and for example, all the morphological and kinematic plots of § 5 are practically unaltered if $i = 48°$ is used instead of $i = 52°$.

In conclusion, our simulation models seem to explain quite well the large difference between kinematic and isophotal orientations. The best fit between simulated and observed stellar isophotes is obtained for $(\phi, i) = (170°, 48°)$. For $A \approx 0.75$ the difference as compared with the kinematic determination in Paper I is simultaneously accounted for.

7. SUMMARY AND CONCLUSIONS

We have performed a fairly extensive survey of gas morphology and kinematics in the nonaxisymmetric gravitational potential of IC 4214, as derived from H-band observations (Paper I). The experiments were performed with two-dimensional simulations employing dissipatively colliding particles in a rigidly rotating bar + spiral potential. Comparisons to "live" two-dimensional simulations indicate that the method should be able to constrain the major bar characteristics (pattern speed and amplitude) with reasonable accuracy. The main uncertainties in the potential evaluation are the unknown vertical extent of the bar and the exact orientation of the galaxy as seen on the sky. However, the latter uncertainty could be significantly reduced during the simulation survey. The potential model used agrees fairly well with the axisymmetric rotation curve (Paper I) and can be derived from the overall H-band luminosity distribution with a constant mass-to-luminosity ratio $M/L_H \approx 0.75$, provided that IC 4214 has a small-mass central region with high H-band luminosity. However, all our conclusions are insensitive to the assumptions concerning the central regions.

Runs with different bar amplitudes and pattern speeds were performed. Bar amplitudes were measured relative to a nominal strength obtained by assuming that the ratio of bar

vertical scale/exponential scale length is about 1/6 and that the observed rotation curve follows from the mass seen in the H-band image. Morphological comparisons, especially those comparing the inner ring morphology with the Hα and $U-I$ images (see Paper I), suggest that the bar strength is most probably about 75% of this nominal amplitude ($A \approx 0.75$). For $A \approx 1$ the inner ring gets excessively peaked and almost disappears if $A > 1$, whereas for much smaller A (<0.5) it starts to show multistrand features not seen in observations. However, slightly smaller A (≈ 0.5) would reproduce the B-band morphology of the inner ring quite well. Kinematic perturbations associated with the nonaxisymmetric potential, especially the shifts in the outer zero-velocity line are then too weak as compared with observations. On the other hand, both kinematic perturbations and the simulated ring sizes match the observations very well for $A \approx 0.75$ (the best amplitude depends slightly on $\Omega_{\rm bar}$). A brief survey of closed periodic orbits was also performed, indicating that the simulated morphology is consistent with the appearance of the main orbital families at various bar amplitudes. Other experiments showed that the contribution from other than $m = 2$ and $m = 4$ components is insignificant. The robustness of the obtained morphological features with respect to the assigned impact frequency was also shown. The estimated bar pattern speed, $\Omega_{\rm bar} \approx 35$–$45$ km s^{-1} kpc^{-1}, places corotation somewhat beyond its outer end ($r_{\rm bar}/r_{\rm cr} \approx 0.67$–$0.77$), in general agreement with several previous studies of early-type galaxies.

In a broader context, our extended survey of simulations with various bar amplitudes demonstrates unambiguously the connection between major Lindblad resonances and observed rings in barred galaxies, including the connection between inner rings and the UHR. First, the good correspondence between IC 4214's observed and simulated structure was evident in simulations near the nominal amplitude. Second, the features seen in simulations with reduced A formed a continuous sequence, in both morphology and kinematics. Finally, in the limit of small bar amplitude, simulated kinematics showed a good one-to-one correspondence to a linear analytical calculation including the resonance terms arising from the $m = 2$ and $m = 4$ components of the nonaxisymmetric potential.

The fact that the nominal strength of the bar was found to be slightly too high has in principle at least three alternative explanations: (1) the bar is thicker than assumed, (2) some part of the total force is accounted for by unseen material, and (3) H-band luminosity is not a reliable tracer of mass density contrast. The first explanation alone appears insufficient, as our nominal bar strength $A = 1$ already assumes a quite substantial three-dimensional thickness, about twice that obtained in near-IR studies of edge-on galaxies. To account for $A = 0.75$, the bar vertical scale should be almost one-half of the radial scale length. The possibility that some unseen halo material contributes to the rotation curve seems likely. However, its distribution must be such that it yields a rather similar rotation curve as that due to the disk. The third explanation, that the azimuthal variations in the H-band overestimate the overall mass contrast, perhaps due to concentration of young objects on the bar and spiral arms, thus seems unnecessary.

It is of interest to compare the estimated amount of IC 4214's unseen halo with simulation studies that have addressed the slowing down of a bar as a result of interaction between the bar and the halo. Debattista & Sellwood (1998) have shown that if $F_{\rm disk}/F_{\rm halo} < 4$ at two disk scale lengths, angular momentum transfer from bar to halo will slow the bar so that $r_{\rm bar}/r_{\rm cr} < 0.7$. On the other hand, the halo material outside the bar region is less important. Our best model with $\Omega_{\rm bar} = 40$ km s^{-1} kpc^{-1}, $A = 0.75$ has $r_{\rm bar}/r_{\rm cr} = 0.72$ and $F_{\rm disk}/F_{\rm halo} \approx 0.75/(1 - 0.75) \approx 3$, which is marginally consistent with their result. A slightly increased A would still be well within the accuracy of our morphological and kinematic comparisons. Also, if a somewhat thicker bar is assumed, for example if $z_0/r_e = 1/4$ instead of 1/6, the nominal amplitude decreases by about 8%, and even for $A = 0.75$ we obtain $F_{\rm disk}/F_{\rm halo} \approx 0.75/(0.92 - 0.75) \approx 4.5$. Thus, taking into account various uncertainties our modeling results agree with Debattista & Sellwood's simulations. In fact, the same argument can also be applied to further support our preferred value $\Omega_{\rm bar} = 40$ km s^{-1} kpc^{-1}. Namely, in § 5.2 it was shown that for a somewhat faster bar an acceptable match could be obtained if the bar amplitude is reduced. However, unless an unrealistically thick bar is assumed, this implies larger halo contribution, which contradicts Debattista & Sellwood's result. Similarly, for a slightly slower bar, no halo at all would be necessarily needed: this would however leave open the question of what has caused the slow rotation rate.

The main defects remaining in our model are the orientation of the nuclear ring and the lack of spiral features inside the inner ring. The simulated nuclear ring was practically perpendicular to the bar major axis, whereas the observed nuclear ring leads by about 50° with respect to the bar. The lack of spiral features could simply be due to a lack of physics in our model (e.g., omission of star-gas recycling), whereas the orientation of the central oval might indicate that IC 4214 could have a nuclear bar that has a different pattern speed from the main bar and thus a random orientation. The orientation of the nuclear ring would then be due to this bar or its combined effect with the main bar. Maciejewski & Sparke (1997) have also demonstrated the existence of closed orbits in potentials having two bar components. However, no signs of a nuclear bar were seen in observations (Paper I). The present simulations indicate an alternative possibility: in high-viscosity simulations, the nuclear ring had a tendency to librate considerably, sometimes deviating even 20% from the perpendicular orientation with respect to the bar. However, this might be an artifact related to the sticky particle simulation method.

In addition, we used the simulation models to address the discrepancy between standard kinematic and isophotal orientation determinations. Qualitatively this discrepancy is exactly what can be expected in the case where methods appropriate for axisymmetric disks are applied to a barred galaxy with strong morphological and kinematic distortions. However, we were able to explain quantitatively the about 10° shift in i and the about 5° shift in ϕ. These considerations also lead to a revised inclination value.

In the future we plan to apply similar methods to other galaxies with near-IR data and good-quality Fabry-Perot velocity fields. Also, self-consistent models with live three-dimensional bars will be studied.

We thank an anonymous referee for many helpful comments that improved the quality of this paper. H. S. acknowledges financial support from the Academy of Finland. R. B., G. B. P., and D. A. C. acknowledge the

support of NSF grants AST 90-14137 and AST 96-17154 to the University of Alabama. M. L. C. acknowledges the support of NSF Research Experiences for Undergraduates (REU) grant AST 94-24226 to the University of Alabama.

REFERENCES

Athanassoula, E. 1984, Phys. Rep., 114, 319
———. 1992a, MNRAS, 259, 328
———. 1992b, MNRAS, 259, 345
Ball, R. 1992, ApJ, 395, 418
Barnaby, D., Thoronson, H. A., Jr. 1992, AJ, 103,41
Binney, J., & Tremaine, S. 1987, Galactic Dynamics (Princeton: Princeton Univ. Press)
Buta, R. 1995, ApJS, 96, 39
Buta, R., & Combes, F. 1996, Fundam. Cosmic Phys., 17, 95
Buta, R., Purcell, G. B., Lewis, M., Crocker, D. A., Rautiainen, P., & Salo, H. 1998, AJ, 117, 778 (Paper I)
Buta, R., van Driel, W., Combes, F., Wakamatsu, K., Sofue, Y., & Tomita, A. 1995, ApJ, 450, 593
Byrd, G., Rautiainen, P., Salo, H., Buta, R., & Crocker, D. A. 1994, AJ, 108, 476
Combes, F., & Elmegreen, B. G. 1993, A&A, 271, 391
Combes, F., & Gerin, M. 1985, A&A, 150, 327
Contopoulos, G. 1980, A&A, 81, 198
Contopoulos, G., & Grosbøl, P. 1989, A&A Rev., 1, 261
Debattista, V. P., & Sellwood, J. A. 1998, ApJ, 493, L5
Duval, M. F., & Athanassoula, E. 1983, A&A, 121, 297
Elmegreen, B. G. 1996, in ASP Conf. Ser. 91, Barred Galaxies, ed. R. Buta, D. A. Crocker, & B. G. Elmegreen (IAU Colloq. 157) (San Francisco: ASP), 197
Elmegreen, D. M., & Elmegreen, B. G. 1995, ApJ, 445, 591
England, M. N. 1989, ApJ, 344, 669
Friedli, D., & Benz, W. 1995, A&A, 301, 649
Hänninen, J., & Salo, H. 1994, Icarus, 108, 325
Hunter, J. H., Ball, R., Huntley, J. M., England, M. N., & Gottesman, S. T. 1988, ApJ, 324, 721
Kent, S. M. 1986, AJ, 91, 301
Lindblad, P. A. B., & Kristen, H. 1996, A&A, 313, 733
Lindblad, P. A. B., Lindblad, P. O., & Athanassoula, E. 1996, A&A, 313, 65
Little, B., & Carlberg, R. G. 1991, MNRAS, 250, 161
Maciejewski, W., & Sparke, L. S. 1997, ApJ, 484, L117
Masset, F., & Tagger, M. 1997, A&A, 322, 442
Oliva, E., Origlia, L., Kotilainen, J. K., & Moorwood, A. F. M. 1995, A&A, 301, 55
Ostriker, J. P., & Peebles, P. J. E. 1973, ApJ, 186, 467
Patsis, P. A., Athanassoula, E., & Quillen, A. C. 1997, ApJ, 483, 731
Pence, W. D., & Blackman, C. P. 1984, MNRAS, 210, 547
Piner, B. G., Stone, J. M., & Teuben, P. J. 1995, ApJ, 449, 508
Quillen, A. C. 1996, in ESO/MPA Workshop, Spiral Galaxies in the Near-IR, ed. D. Minniti & H.-W. Rix (Berlin: Springer), 157
Raha, N., Sellwood, J. A., James, R. A., & Kahn, F. D. 1991, Nature, 352, 411
Rautiainen, P., & Salo, H. 1998, in preparation
Rice, W., Merrill, K. M., Gatley, I., & Gillett, F. C. 1996, AJ, 112, 114
Salo, H. 1991, A&A, 243, 118
Salo, H., & Laurikainen, E. 1993, ApJ, 410, 586
Saraiva, M. F. 1997, AJ, 113, 1607
Schwarz, M. P. 1981, ApJ, 247, 77
———. 1985, MNRAS, 212, 677
Sellwood, J. A. 1981, A&A, 99, 362
———. 1987, ARA&A, 25, 151
———. 1996, in ASP Conf. Ser. 91, Barred Galaxies, ed. R. Buta, D. A. Crocker, & B. G. Elmegreen (IAU Colloq. 157) (San Francisco: ASP), 309
Sellwood, J. A., & Sparke, L. S. 1988, MNRAS, 231, 25P
Sellwood, J. A., & Wilkinson, A. 1993, Rep. Prog. Phys., 56, 173
van Albada, T. S., & Sanders, R. H. 1982, MNRAS, 201, 303
van der Kruit, P. C., & Searle, L. 1982, A&A, 110, 79
Warner, P. J., Wright, M. H. C., & Baldwin, J. E. 1973, MNRAS, 163, 163